FAILURE MODELING AND LIFE PREDCITION OF RAILROAD WHEELS

By

Venkata Sasidhar Sura

Dissertation

Submitted to the Faculty of the

Graduate School of Vanderbilt University

in partial fulfillment of the requirements

for the degree of

DOCTOR OF PHILOSOPHY
in

Civil Engineering

December, 2011

Nashville, Tennessee

Approved:

Professor Sankaran Mahadevan

Professor Prodyot K. Basu

Professor Caglar Oskay

Professor Carol Rubin

To my family

ACKNOWLEDGEMENTS

This research would not have been possible without the help from several people. First, I would like to thank my committee members, Prof. Sankaran Mahadevan, Prof. Prodyot K. Basu, Prof. Caglar Oskay, and Prof. Carol Rubin for their valuable guidance and suggestions. I owe special thanks to my advisor Dr. Mahadevan for mentoring and supporting me throughout this research. I feel extremely fortunate for getting a chance to be a part of his research group. Working with him has been a great learning experience to me both professionally and personally. I hope that I can emulate at least some of his great qualities, which are too many to list.

I would also like to express my gratitude to my project sponsors and project monitors: Scott Cummings, Francisco Robles, and Semih Kalay, Transportation Technology Center, Inc., Steve Dedmon and James Pilch, Standard Steel, LLC, John Oliver, Griffin Wheel Company. The financial support and valuable discussions are gratefully acknowledged. I would also like to thank Dr. Yongming Liu, Clarkson University, for his mentoring during the initial stages of this research.

On a personal note, I would like to thank my parents and brother for their love and support throughout my life. Finally, I would like to thank my friends at Vanderbilt for their great friendship and making my stay at Vanderbilt a very pleasant experience.

TABLE OF CONTENTS

Page

LIST OF TABLES

LIST OF FIGURES

CHAPTER 1

INTRODUCTION

1.1 Motivation

Railroad wheel failures can lead to train derailments and cost billions of dollars to the railroad industry. Therefore, it is important to understand how different types of wheel failures occur in order to develop effective risk management procedures. Most of the research in the literature on estimating the wheel failure life uses a conservative safe-life design approach, whereas the current research uses the damage-tolerance approach, which is more economically beneficial, in estimating the wheel failure life. However, this requires accurate fracture mechanics analysis. Previous studies in this direction have developed limited analysis options and often considered only a single type of wheel failure (either fatigue failure or wear failure) in estimating the failure life. The current study develops an advanced analysis methodology to estimate the wheel failure life under realistic service conditions and considering multiple failure types. Also, probabilistic analysis is performed to consider uncertainties in service conditions.

1.2 Introduction

Railroad wheel rim damage occurs due to both fatigue and wear failure mechanisms. In recent years, increased train speeds and axle loads have increased the contact stresses, thereby changing the major wheel rim damage mechanism from wear to fatigue [1]. The fatigue problem of railroad wheels, referred to as rolling contact fatigue [2], is caused by

repeated contact stress during the rolling motion. An overview of rolling contact fatigue is given in [3]. Three important wheel rim failure mechanisms are shattered rim, vertical split rim, and thermal damage (shelling / spalling) [4].

This research focuses on modeling shattered rim and vertical split rim cracking. Shattered rim cracks initiate from deep sub-surface defects; once initiated these cracks propagate roughly parallel to the tread surface, and failure occurs when the crack reaches the surface and a piece of the wheel is broken off. Vertical split rim cracks initiate from shallow sub-surface defects or shelling/spalling cracks; once initiated these cracks propagate roughly parallel to the front rim face or back rim face, and failure occurs when the crack reaches the surface and a part of the wheel is broken off.

This research considers realistic service conditions in modeling these two types of cracking. Since the residual stresses developed during the manufacturing process or under service conditions can affect the contact stresses, thereby affecting the wheel failure life, the current research includes residual stresses as initial stresses for rolling contact analysis. Residual stresses developed due to both the manufacturing process and the service conditions are estimated using decoupled thermal-structural finite element analyses. The computed residual stresses are validated using experimental data.

This research investigates the effect of various parameters, such as wheel geometry (rim thickness), residual stresses, load characteristics (location and magnitude), crack characteristics (size and location), and wheel wear on both shattered rim and vertical split

rim cracking. The most critical parameters that can trigger a shattered rim or vertical split rim failure are identified. This research estimates the wheel failure life probabilistically, considering uncertainties from several sources and considering multiple failure types. The computed results are validated with field data.

1.3 Objectives

This study combines structural failure analysis, finite element analysis, fracture mechanics, and reliability analysis methods to develop a new methodology to analyze and simulate railroad wheel failure. This research is divided into four objectives as follows:

1. Modeling of sub-surface cracking in railroad wheels
2. Inclusion of residual stresses and wheel wear
3. Investigating the effect of various parameters on sub-surface cracking, and
4. Probabilistic failure life prediction

The first objective simulates sub-surface cracking in railroad wheels using finite element analysis and fracture mechanics concepts. A shattered rim failure or a vertical split rim failure can occur due to sub-surface cracking. Shattered rim cracking occurs due to the initiation of cracks from deep sub-surface defects and propagation of these cracks approximately parallel to the tread surface. Vertical split rim cracking occurs due to the initiation of cracks from shallow sub-surface defects or due to shelling/spalling cracks and propagation of these cracks approximately parallel to the front rim face or back rim

face. Vertical split rim cracks can also form due to kinking of shallow sub-surface cracks parallel to the tread surface. This research considers only vertical split rim cracks that are parallel to the front rim face. For computational efficiency, finite element analysis is divided into two stages: full model analysis and sub-model analysis. In the full model analysis, a 3D finite element model of a railroad wheel without any sub-surface fatigue crack is considered and rolling contact analysis is performed. In the sub-model analysis, a 3D finite element model of a small block with an embedded fatigue crack is considered and the results from the full model are used as inputs to the sub-model to estimate the uni-modal stress intensity factors at the crack tip. The equivalent stress intensity factor range (ΔK_{eq}) at a crack tip is estimated using the uni-modal stress intensity factors obtained from the finite element analysis and a mixed-mode crack growth model based on critical plane concepts. These estimated ΔK_{eq} values can help in better understanding of shattered rim and vertical split rim cracking.

The second objective estimates the residual stresses that develop in a railroad wheel due to various sources and also considers wheel wear. Residual stresses develop in a wheel during the manufacturing process due to the rim quenching. Residual stresses also develop due to thermal brake loading under service conditions as the wheel also functions as a brake drum in addition to supporting the mechanical loads. Residual stresses developed during both the manufacturing process and under service conditions are estimated using transient thermal analysis and non-linear elastic-plastic structural analysis. Service-induced residual stress is estimated considering the estimated as-manufactured as initial stress. This research also considers wheel wear. Wheel wear is the

process of surface material removal under service conditions. Uniform wheel wear is assumed in this reserach for the sake of computational ease. The wheel profile with a thinner rim thickness is obtained by imposing the tread surface at the required rim thickness. Since wheel wear removes the surface material and the residual stresses in the outer strip, the as-manufactured residual stress in a thinner rim thickness wheel is not identical to that of a new wheel. The as-manufactured residual stress component in a thinner rim wheel is estimated using decoupled thermal-structural analysis and sub-modeling techniques. This estimated as-manufactured residual stress component is considered as initial stress in estimating the service-induced residual stress in a thinner rim thickness wheel.

The third objective investigates the effect of various input parameters on shattered rim and vertical split rim cracking. The equivalent stress intensity factor ranges (ΔK_{eq}) at shattered rim and vertical split rim crack tips are estimated using the methodology developed in the first Chapter. The effect of several input parameters, such as load characteristics (location and magnitude), crack characteristics (lateral location, vertical location, and size), residual stresses, and wheel geometry on shattered rim cracking and vertical split rim cracking is investigated and the critical parameters that can trigger a shattered rim and vertical split rim failure are identified.

The fourth objective predicts the probabilistic railroad wheel failure life considering both shattered rim and vertical split rim under realistic service conditions. Realistic loading conditions are simulated by considering variable amplitude wheel loading. Load histories

obtained from wheel impact load detectors (WILD) are considered and applied on the tread surface as block loading. The lateral load location is varied to simulate the contact conditions that can occur when a wheel traverses over a curve. Sub-surface cracks of different sizes are considered in the rim and the lateral and vertical crack locations are assumed to be randomly distributed. Shattered rim cracks and vertical split rim cracks are simulated by considering different crack orientations. An equivalent initial flaw size is considered to bypass the short crack growth region and to be able to use a long crack growth model for failure life prediction. A computationally inexpensive surrogate model is constructed to replace expensive finite element simulations for calculating the ΔK_{eq} at the crack tip. The wheel failure life is estimated using the ΔK_{eq} values obtained from the surrogate model and a long crack growth model. The lower of the shattered rim and vertical split rim failure lives is reported as the failure life. Monte Carlo simulations are performed to obtain the distribution of failure life. Multiple sets of Monte Carlo simulations are performed to obtain the scatter in computed results. The simulation results are validated with field data.

CHAPTER 2

MODELING OF SUB-SURFACE CRACKING IN RAILROAD WHEELS

2.1. Introduction

This Chapter focuses on modeling shattered rim and vertical split rim cracking as these are observed to be the two most dominant failure types in North America. This Chapter simulates these two types of cracking using a three-dimensional, multi-resolution, elastic-plastic finite element model. Rolling contact loading is simulated by applying the wheel load on the tread surface is applied as a parabolic pressure distribution over the Hertzian contact area. The equivalent stress intensity factor (ΔK_{eq}) ranges at sub-surface crack tips are estimated using uni-modal stress intensity factors obtained from the finite element analysis and a mixed-mode crack growth model based on critical plane approach. The methodology developed in this Chapter to estimate the ΔK_{eq} at a crack tip will be useful in predicting the railroad wheel failure life due to these two types of failures.

Shattered rim failures are the result of large sub-surface fatigue cracks that propagate roughly parallel to the wheel tread surface [5,6]. These cracks generally initiate from voids in cast wheels and from aluminum oxide inclusions in forged wheels, propagate and destroy the wheel's integrity, and lead to train derailments at higher speeds [7]. A shattered rim crack usually initiates under a very high wheel load, such as an impact load, and propagates even under regular service loading [7]. Figure 1 shows a typical shattered rim failure.

Figure 1. Typical shattered rim failure [7].

In the literature, most of the research on shattered rim failure has been focused on understanding the shattered rim crack initiation from material defects [8-12]. These studies can be broadly classified into two groups: (1) experimental studies, and (2) modeling and simulation-based studies.

Among experimental studies, Stone and Dahlman [8] provided micrographic evidence for a shattered rim crack initiation from a void of size 0.64 mm (0.025 in). Baretta et al. [9] estimated the typical dimensions of aluminum oxide inclusion in wrought wheel for shattered rim crack initiation have a length of 1 to 5 mm (0.04 to 0.2 in) and width of 0.3 to 1 mm (0.012 to 0.04 in).

Among modeling and simulation based studies, Ekberg et al. [10] argued that pores are the worst type of inclusions; therefore, material defects can be modeled as pores. Ekberg

et al. [10] modeled pores as circular holes and performed numerical simulations using a 2-D finite element model. From the numerical results, it was concluded that the complex stress response close to the defect depends on the applied load and the defect location. Lunden [11] modeled material defects as cracks, and studied the crack initiation and propagation in the contact region of a railway wheel using analytical and numerical methods assuming Hertzian contact pressure. A 2-D finite element model with a mathematically sharp crack was considered. From the results, the maximum allowable defect size to prevent failure was estimated to be 1 mm (0.04 in). Marais [11] estimated the maximum allowable defect size to prevent shattered rim failure as 1 mm (0.04 in) using Hertzian contact theory and a fatigue damage model.

Vertical split rim failure occurs due to rapid shallow sub-surface crack propagation with a piece of either a front or back of the rim breaking off the wheel. The vertical split rim crack can originate from existing tread damage (such as shell or spall cracks) or from a very shallow sub-surface crack [13]. The unstable propagation of a vertical split rim crack is believed to be triggered under wheel impact loading. Wheel impact loads can occur due to surface defects on the tread surface or due to track conditions, such as crossing diamonds [14]. Figures 2(a) and 2(b) show typical vertical split rim failures with a piece of the front rim and the back rim broken off respectively [15].

(a) (b)

Figure 2. Typical vertical split rim failures [10]

In the literature, very limited research has been reported related to the vertical split failure in railroad wheels. Lonsdale et al. [14] performed both computational and experimental work to understand the stress levels in the wheel rim under an impact load. This Chapter found that the load location close to the front rim face generates higher stresses in the rim. The finite element results estimated the axial stresses on the wheel tread surface along the taping line as tensile stresses with magnitudes of 200 MPa (29 ksi) and 393 MPa (57 ksi) for wheels with rim thicknesses 38.1 mm (1.5 in) and 22.225 mm (0.875 in) respectively, under an impact load of 890 kN (200 kips) at 25.4 mm (1 in) from the front rim face. However, drop tests with a load of 890 kN (200 kips) on a wheel with a rim thickness of 31.75 mm (1.25 in) did not trigger a vertical split rim failure.

Stone et al. [10] discussed the effects of residual stress, wheel geometry, and loading characteristics on vertical split rim failure. This Chapter suggested that the vertical spilt rim failure occurs due to high bending stresses developed in the rim. These high bending

stresses can develop due to track conditions (wheel riding over a curve) or due to wheel conditions (false flange and hollow tread). The field inspection of 24 broken wheels failed due to vertical split rim cracking revealed that the failures were initiated from shell cracks at a depth of 2.5 mm (0.1 in) below the tread surface and the rim thickness did not appear to be a critical parameter in triggering this failure. The contribution of residual stress to the total stress for vertical split rim failure was calculated as approximately 15%. This Chapter performed a two dimensional analysis using only bi-axial stresses and recommended a detailed three dimensional finite element analysis for better understanding of vertical split rim failure.

A couple of Canadian derailment reports [16, 17] mention vertical split head failures in rails as the cause of train derailments. The vertical split head failure mechanism of the rail appears to be similar to the vertical split rim failure of the wheel. However, wheels are different and more complex compared to rails due to difference in geometry, and the presence of braking and residual stresses. In these reports, it was mentioned that vertical split heads propagate very rapidly and fail suddenly without any warning. It was also mentioned that the high vertical loads (probably impact loads) are responsible for the vertical split head failures.

This Chapter develops an advanced computational model to simulate shattered rim and vertical split rim cracking under rolling contact loading. For computational efficiency, the finite element model is divided into two levels: full model and sub-model. In the full model, the 3D wheel geometry without any fatigue crack is considered and rolling

contact analysis is performed. In the sub-model, a small block with an embedded fatigue crack is considered and the uni-modal stress intensity factors at the crack tip are estimated. The equivalent stress intensity factor range (ΔK_{eq}) at the crack tip is estimated using uni-modal stress intensity factor values obtained from finite element analysis and a mixed-mode crack model based on critical plane concepts. The methodology developed in this Chapter to estimate ΔK_{eq} at a shattered rim or vertical split rim crack tip will be useful in better understanding of these failures and to predict the failure life due to these two types of failures.

2.2 Methodology

The proposed methodology to model shattered rim and vertical split rim cracking consists of two parts: (1) finite element analysis and (2) mixed-mode crack model to estimate the ΔK_{eq}

2.2.1 Finite element analysis

The sub-surface cracking in railroad wheel rims is modeled using a three-dimensional finite element model. For computational efficiency, the finite element analysis is divided into two steps: full model analysis and sub-model analysis.

2.2.1.1. Full model analysis

In full model analysis, a three-dimensional finite element model of a railroad wheel is considered and rolling contact loading is simulated by applying the wheel load on the tread surface and performing elastic-plastic structural analysis. This Chapter assumes constant amplitude wheel loading and the load location to be along the taping line. Variable amplitude wheel loading and various lateral load locations will be considered in

later Chapters. Elastic-plastic structural analysis is performed using the finite element full model to estimate contact stresses and stresses in the wheel rim under constant amplitude wheel loading.

Figure 3 shows the full model developed using ANSYS [18]. This finite element model is constructed using cylindrical co-ordinate system, with X-axis along the radial direction, Y-axis along the axial direction, and Z-axis along the circumferential direction.

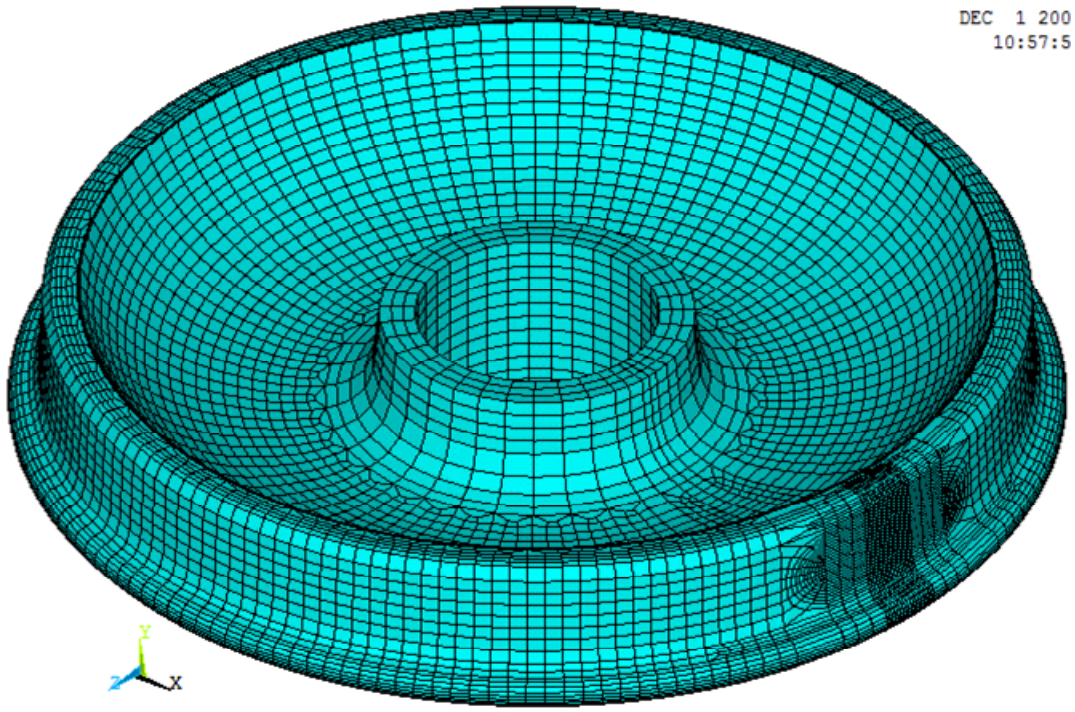

Figure 3. Finite element model of a railroad freight car wheel

This finite element full model is meshed using SOLID185 elements, which are 8 node elements with three translational degrees of freedom at each node. The mesh is refined over the wheel tread surface where the mechanical load (high wheel load) is to be applied. The mechanical load along the taping line is applied as contact pressure on the

tread surface over a Hertzian contact area. The Hertzian contact area depends on the transverse profile radii of the wheel and the rail, the applied load and the material properties. The contact pressure over the Hertzian contact area is applied as a parabolic distribution with the maximum value at the center of the contact area and tapering down to zero along the boundary of the elliptical contact area [19]. Liu and Mahadevan [51,52] modeled rolling contact loading using three-dimensional rail-wheel finite element model and found that the contact stresses and stresses in the rim are close to those of Hertzian contact analysis. Since it is computationally very expensive to model rolling contact loading using rail-wheel finite element model, this research uses Hertzian contact analysis. Figures 4 a-b shows the refined mesh in the wheel rim and the parabolic contact pressure distribution centered along the taping line on the tread surface.

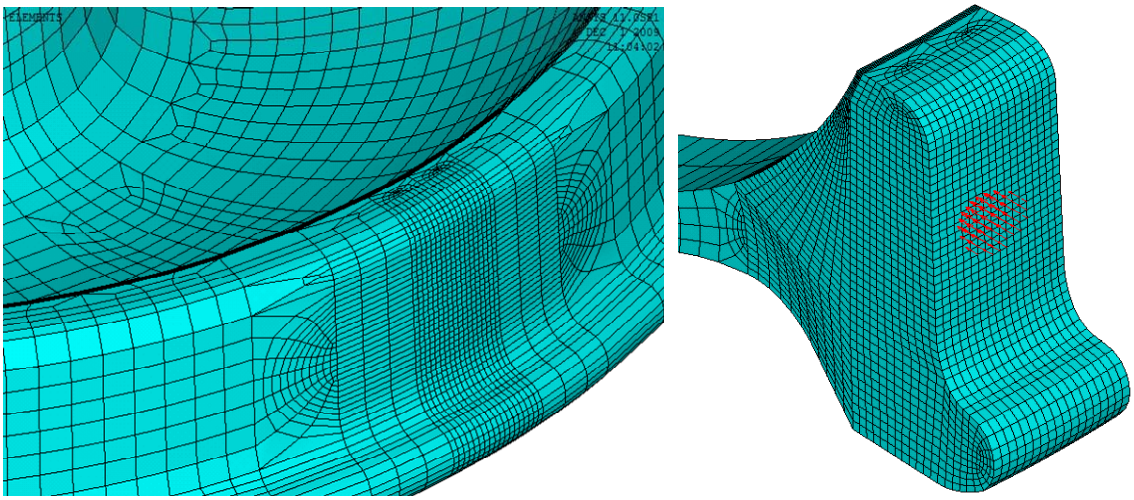

(a) (b)

Figure 4(a). Refined mesh in the wheel rim; Figure 4(b). Parabolic contact pressure distribution on the tread surface

The full model analysis is performed using elastic-plastic finite element analysis and the contact stresses and stresses in the wheel rim under constant amplitude wheel loading is estimated. The results from the full model analysis are considered as the input for the sub-model analysis.

2.2.1.2 Sub-model analysis

In the sub-model analysis, a small block with an embedded circular mathematically sharp crack is considered. This block can be considered as either a shattered rim or vertical split rim crack initiation site. The sub-surface cracking, either shattered rim or vertical split rim cracking, can be simulated by placing this block at the desired location in the wheel rim. In other words, the shattered rim or vertical split rim cracking can be simulated by appropriately aligning the sub-model to the desired orientation and applying the results from the full model at that location as boundary conditions to the sub-model. The sub-model analysis calculates uni-modal stress intensity factors at a sub-surface crack tip.

Figures 5 a-b show the finite element details of the sub-model constructed in ANSYS. The finite element sub-model mesh consists of SOLID185 elements, similar to that of the full model. This sub-model consists of 15,501 nodes and 9,152 elements. The element size along the boundary of the sub-model is about 3 mm (1/8 in) and the element size along the crack front (shown as black curve in Figure 5 (b)) is about 1/20 th of the crack size. The elements along the crack front are modified from SOLID185 to SOLID186 elements with quarter point node locations to model the stress singularity along the crack front. The top and bottom crack surfaces are modeled as contact surfaces using

CONTA173/CONTA174 and TARGE170 elements to avoid penetration of one surface into the other under a compressive load. The full model results are applied as boundary conditions to the sub-model. The uni-modal stress intensity factors for all the three modes I, II, and III (K_I, K_{II}, and K_{III}) are calculated using elastic-plastic finite element analysis.

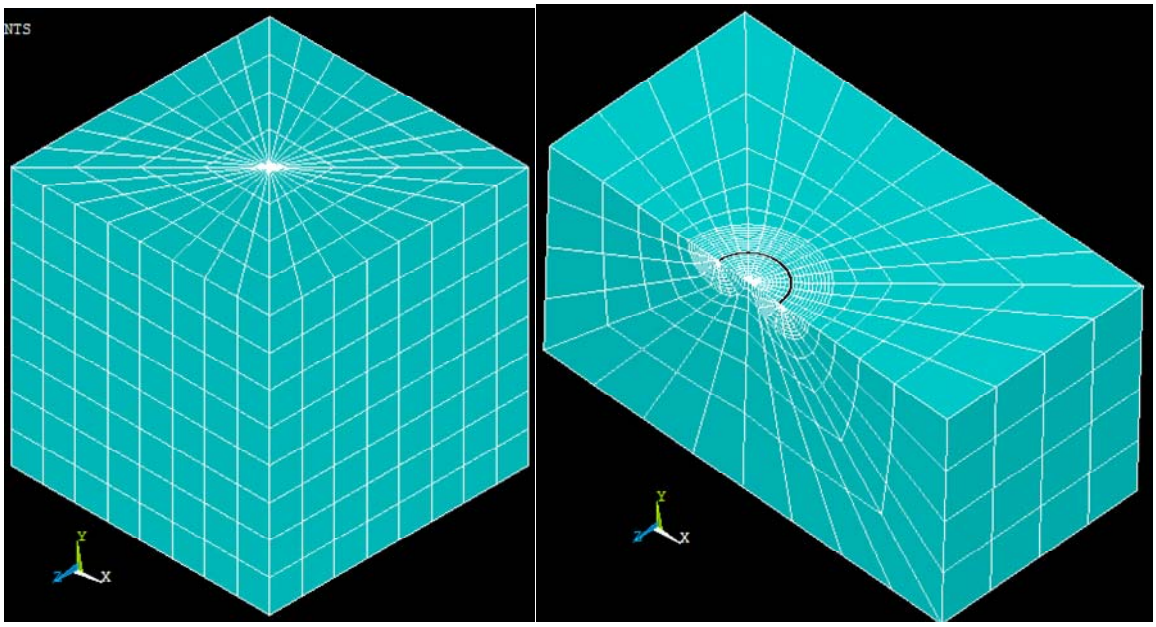

(a) Complete sub-model (b) Quarter portion of the sub-model

Figure 5. Finite element sub-model with an embedded circular fatigue crack.

2.2.2 Mixed-mode equivalent stress intensity factor calculation

A fracture mechanics-based threshold mixed-mode crack model developed by Liu and Mahadevan [20] is used in this Chapter. This model is derived using a mixed-mode fatigue damage model based on critical plane concepts [21] and the El Haddad's model [22]. In the critical plane-based mixed-mode fatigue damage model, the damage is evaluated on the critical plane. This critical plane is obtained by minimizing the hydrostatic stress. The various steps to identify the critical plane at a given location in a component subjected to multi-axial loading are described here in brief.

At a given location, a numerical search is performed to identify the plane with maximum normal stress amplitude. Since this is the plane along which the actual fracture happens, this plane is called fatigue fracture plane. This plane is shown in Figure 6. The plane with axis 1' as normal is the fatigue fracture plane. Once the fatigue fracture plane is identified, a numerical search is performed to identify the maximum shear stress amplitude direction on this fatigue fracture plane. The axis 2' represents the maximum shear stress amplitude direction on the fatigue fracture plane. The axis that is normal to both 1' and 2' is called 3'. The fatigue fracture plane is rotated about axis 3' by an angle γ to obtain the critical plane, where the hydrostatic stress is minimum. The multi-axial fatigue damage is evaluated on this critical plane. Eq. (1) shows the multi-axial fatigue damage model

$$\sqrt{\left(\frac{\sigma_{a,c}}{f_{-1}}\right)^2+\left(\frac{\tau_{a,c}}{t_{-1}}\right)^2+A\left(\frac{\sigma^H_{a,c}}{f_{-1}}\right)^2}=B \qquad (1)$$

where $\sigma_{a,c}$ is the normal stress amplitude on the critical plane, $\tau_{a,c}$ is the shear stress amplitude on the critical plane, $\sigma^H_{a,c}$ is the hydrostatic stress on the critical plane, f_{-1} is the tensile fatigue limit of a smooth specimen, t_{-1} is the shear fatigue strength of a smooth specimen, and A and B are material parameters.

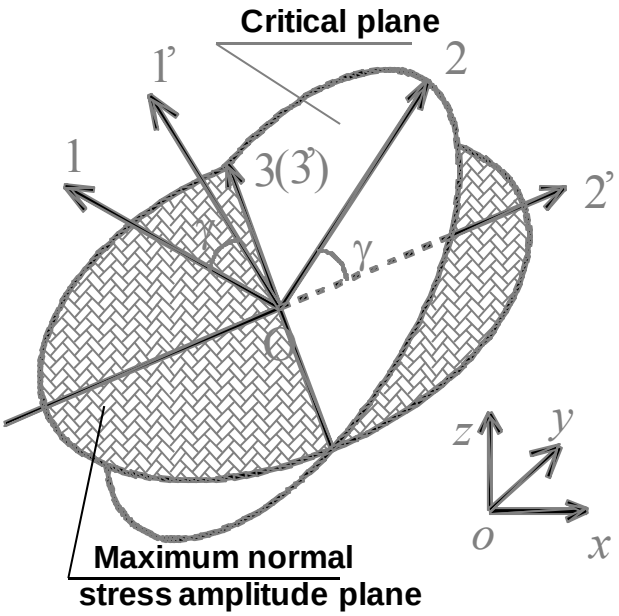

Figure 6. Illustration that shows the fatigue fracture plane and the critical plane

In the safe-life design approach, fatigue limit is used to define loading conditions under which a component does not fail indefinitely. In damage tolerant design, threshold stress intensity factor range is used as the criterion to define loading conditions that do not propagate fatigue cracks, and thereby making the component not fail indefinitely. El Haddad's [22] model describes the relationship between fatigue limit and the threshold stress intensity factor range using a fictional crack length *a,* which is shown in Eq. (2)-(3).

$$f_{-1} = \frac{\Delta K_{th,I}}{\sqrt{\pi a}} \tag{2}$$

$$\tau_{-1} = \frac{\Delta K_{th,II}}{\sqrt{\pi a}} or \tau_{-1} = \frac{\Delta K_{th,III}}{\sqrt{\pi a}} \tag{3}$$

The crack length *a* represents the intersection of the smooth specimen fatigue limit and linear elastic fracture mechanics (LEFM) fatigue threshold in Kitagawa diagram [56]. Figure 7 shows the Kitagawa diagram.

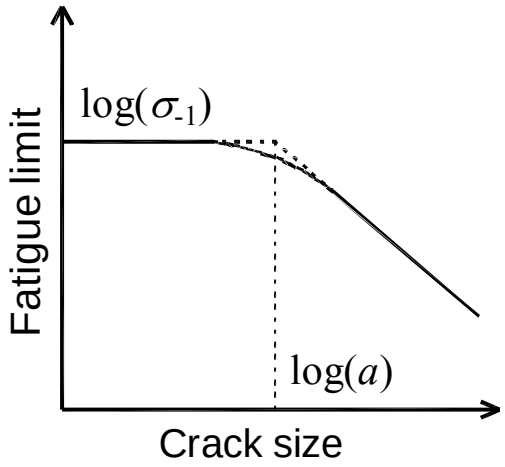

Figure 7. Kitagawa diagram

By substituting Eq. (2) – (3) in Eq. (1), the expression for a threshold mixed-mode crack model can be obtained. The details of the derivation and validation are given in [20]. Only a brief description of this model is given in this Chapter.

The threshold mixed-mode crack model derived in [20] gives an expression for calculating the equivalent stress intensity factor range at the crack tip (ΔK_{eq}) based on the uni-modal stress intensity factor ranges and material properties, which is shown in Eq. (4).

$$\Delta K_{eq} = \frac{1}{B}\sqrt{(\Delta k_1)^2 + (\frac{\Delta k_2}{s})^2 + (\frac{\Delta k_3}{s})^2 + A(\frac{\Delta k^H}{s})^2} = f(\frac{da}{dN}) \quad (4)$$

where ΔK_{eq} is the equivalent stress intensity factor range under mixed-mode loading. $f(\frac{da}{dN})$ is the crack growth curve obtained under mode I loading. Δk_1, Δk_2, Δk_3 and Δk^H are the loading parameters with the same unit as the stress intensity factor. a is the half length of the crack. s is the ratio of mode II and mode I fatigue crack threshold stress intensity factors ($s = \frac{K_{II,th}}{K_{I,th}}$). A larger value of s ($s > 1$) indicates tensile dominated failure and a smaller value of s ($s < 1$) indicates shear dominated failure. A and B are material properties, which are listed in Table 1.

Table 1 Material parameters for fatigue crack propagation prediction [20]

Material Property	$s = \frac{K_{II,da/dN}}{K_{I,da/dN}} < 1$	$s = \frac{K_{II,da/dN}}{K_{I,da/dN}} \geq 1$
γ	$cos(2\gamma) = \frac{-2 + \sqrt{4 - 4(1/s^2 - 3)(5 - 1/s^2 - 4s^2)}}{2(5 - 1/s^2 - 4s^2)}$	$\gamma = 0$
A	$A = 0$	$A = 9(s^2 - 1)$
B	$B = [cos^2(2\gamma)s^2 + sin^2(2\gamma)]^{\frac{1}{2}}$	$B = s$

The equivalent stress intensity factor range at a sub-surface crack tip, either a shattered rim or vertical split rim crack, is estimated using uni-modal stress intensity factor ranges (ΔK_I, ΔK_{II}, and ΔK_{III}) obtained from the finite element analysis and Eq. (4).

2.3 Results and Discussion

A railroad freight car wheel with a diameter of 36 in and a rim thickness of 1.5 in is considered in this study. A wheel load of 50 kips is considered in this Chapter. The mechanical load on the tread surface is applied as a parabolic pressure distribution with the maximum value at the center and tapering down to zero along the boundary of the elliptical contact area. The Hertzian contact parameters, C_a (half contact length along the major axis) and C_b (half contact length along the minor axis) depends on the wheel load for a given wheel geometry. Under a constant amplitude wheel loading of 50 kips, the contact parameters, C_a (along the track direction) is 0.372 in and C_b (along the lateral direction) is 0.294 in. Figure 8 shows the results of full model analysis.

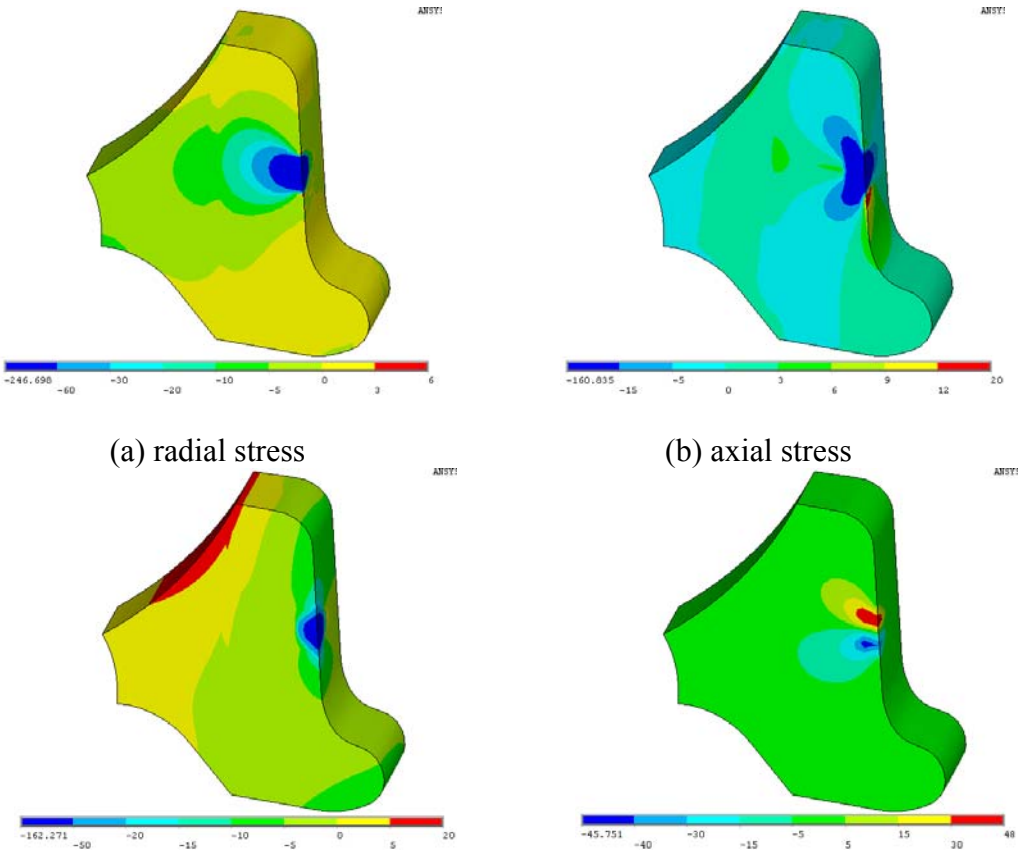

(a) radial stress (b) axial stress

(c) hoop stress (d) shear stress

Figure 8. Full model stress results.

The full model results are applied as boundary conditions for the sub-model analysis for estimating the uni-modal stress intensity factors at a sub-surface crack tip. The finite element sub-model needs to be verified before using it to model sub-surface cracking. This sub-model cracking is verified under all three modes (I, II, and III) by comparing the computed values with those of the stress intensity factor handbook values available in the literature.

The stress intensity factor values at a circular crack tip subjected to remote loading conditions under different modes are given by the Eq. (5) – (7) [24]

$$K_I = \frac{2}{\pi}\sigma\sqrt{\pi a} \tag{5}$$

$$K_{II} = \frac{4}{\pi(2-\upsilon)}\sigma\sqrt{\pi a} \tag{6}$$

$$K_{III} = \frac{4(1-\upsilon)}{\pi(2-\upsilon)}\sigma\sqrt{\pi a} \tag{7}$$

where K_I, K_{II}, and K_{III} are mode I, mode II, and mode III stress intensity factor values, σ is the applied remote stress, ν is the Poisson's ratio, and a is the half crack size.

The finite element sub-model analysis is performed assuming the following parameters: σ = 10 ksi; ν = 0.3; and a = 0.04 in. The finite element analysis estimated the K_I, K_{II}, and K_{III} values as 2.28 ksi√in, 2.66 ksi√in, and 1.83 ksi√in respectively. The corresponding values calculated using Eqs. (5-7) are 2.26 ksi√in, 2.65 ksi√in, and 1.86 ksi√in

respectively. Since the difference between the computed values and the handbook values are small, the finite element sub-model is satisfactorily verified.

2.4 Summary and conclusions

This Chapter developed a methodology to simulate sub-surface cracking, either shattered rim or vertical split rim cracking, using three-dimensional finite element analysis and a mixed-mode crack model based on critical plane concepts. For computational efficiency, finite element analysis is divided into two stages: full model analysis and sub-model analysis. In the full model analysis, a 3D finite element model of a railroad wheel without any sub-surface fatigue crack is considered and rolling contact analysis is performed. The wheel load is considered as constant amplitude loading and is applied on the tread surface using Hertzian contact theory. In the sub-model analysis, a 3D finite element model of a small block with an embedded fatigue crack is considered and the results from the full model are applied as boundary conditions to the sub-model to estimate the uni-modal stress intensity factors at a sub-surface crack tip. The equivalent stress intensity factor range (ΔK_{eq}) at a crack tip is estimated using the uni-modal stress intensity factors obtained from the finite element analysis and a mixed-mode crack growth model based on critical plane concepts. These estimated ΔK_{eq} values can help in better understanding of shattered rim and vertical split rim cracking.

The methodology developed in this Chapter to estimate ΔK_{eq} values at sub-surface crack tips will be used in later Chapters: (1) to investigate the effect of several input parameters, such as load characteristics (location and magnitude), crack characteristics

(lateral location, vertical location, and size), residual stresses, and wheel geometry on shattered rim cracking and vertical split rim cracking, (2) to identify the critical parameters that can trigger a shattered rim failure and vertical split rim failure, and (3) to probabilistically predict the wheel failure life.

CHAPTER 3

RESIDUAL STRESSES AND WHEEL WEAR

3.1 Introduction

Residual stress in wheel rims is one of the important factors that can significantly affect the crack growth rate, and thereby affect the wheel failure life. The shattered and vertical split rim crack growth rates depend on the residual stresses in wheel rims. The axial residual stress developed during the manufacturing process can enhance the vertical split rim crack growth rate and can decrease the vertical split rim failure life [25]. The as-manufactured compressive residual hoop stress inhibits the shattered rim crack growth, and thereby increases the shattered rim failure life [26]. Therefore, consideration of residual stresses helps in better understanding of shattered and vertical split rim cracking. In this Chapter, an advanced computational methodology is developed to estimate residual stresses developed during both the manufacturing process and under service conditions.

Residual stress develops in wheel rims during both the manufacturing process and on-tread braking under service conditions. The residual stress that develops during the manufacturing process is referred to as as-manufactured residual stress [27]. Beneficial compressive residual hoop stress develops in the wheel rim during the manufacturing process. This compressive stress inhibits the crack growth and increases the wheel failure life [26]. The residual stress that develops during the thermal brake loading under service

conditions is referred to as service-induced residual stress [28]. Detrimental tensile residual hoop stress develops during the on-tread braking. This tensile stress enhances the crack growth and decreases the wheel failure life [26]. The final residual stress distribution in wheel rims is the complex combination of these two types of residual stresses.

During the manufacturing process, the wheel is shaped from a cylindrical block through multiple steps of forging, rolling, and pressing. Once the wheel is pressed to the desired shape, it is heated to a temperature of 871 °C (1600 °F) in an austentizing furnace to remove the undesired residual stresses developed during shaping the wheel. Following heating, the wheel is removed from the austentizing furnace and is exposed to room temperature for 90 seconds before performing rim quenching. During rim quenching, water sprays on the tread surface for 5 minutes. Rim quenching develops beneficial compressive residual hoop stress in the rim. Following quenching, the wheel is annealed at a temperature of 860 °F (460 °C) for 4 hours by placing it in an annealing furnace. Annealing increases the toughness and wear resistance. Following annealing, the wheel is allowed to cool down to the room temperature for 6 hours [27].

During rim quenching, the outer rim portion contracts due to the decrease in temperature caused by the water spray. The inner rim portion and plate have lower yield strength compared to that of the outer rim portion as they are at a relatively high temperature. The contraction of the outer rim portion compresses the inner rim portion and plate. This compression leads to compressive yielding in the inner rim portion and plate as they have

reduced yield strength. The inner rim portion and plate deform plastically due to the compressive yielding and are now smaller compared to their original size. When the entire wheel is allowed to cool down, the outer rim portion retains its original size. The inner rim portion and plate are now smaller compared to their original size and are forced to occupy their original space in order to be compatible with the outer rim portion. This constraint develops tensile residual hoop stress in the inner rim portion and plate, and compressive residual hoop stress in the outer rim portion [26].

The additional function of railroad wheels other than supporting mechanical loads is to serve as a brake drum under service conditions. During the on-tread braking, the brake shoes are applied directly on the tread surface. The wheel decelerates due to the friction between the brake shoe and brake drum (wheel). During braking, the kinetic energy of the wheel is dissipated as frictional heat energy. This frictional heat energy develops a temperature gradient in the rim with higher temperatures closer to the tread surface. The amount of frictional heat energy input into the rim depends on the braking duration. The material at the tread surface can be heated to a very high temperature under severe braking conditions, such as descending a grade for longer duration and brake shoes locking onto the tread surface due to malfunction. The thermal brake loading under service conditions develops tensile residual hoop stress in the material at the tread surface [28].

During the on-tread braking, the material at the tread surface is heated to a high temperature due to the frictional heat energy and thus has reduced yield strength. The

hotter material at the tread surface tries to expand; however, it is constrained by the colder inner rim portion and plate. This constraint develops high compressive hoop stress in the material at the tread surface. This compressive hoop stress leads to compressive yielding in the material at the tread surface as it has reduced yield strength. The material at the tread surface deforms plastically due to the compressive yielding and is now smaller compared to its original size. When the entire wheel is allowed to cool down, the inner rim portion and plate occupy their original space. The material at the tread surface, which is now smaller compared to its original size, is forced to occupy its original space in order to maintain the continuity. This constraint develops tensile residual hoop stress in the material at the tread surface. Under severe brake loading, the compressive residual hoop stresses could be reversed to tensile residual hoop stress in the material at the tread surface [26].

The as-manufactured residual stress develops only once for a given wheel as the wheel rim experiences quenching only once in its lifetime. However, the wheel experiences multiple thermal brake loads under service conditions; therefore, service-induced residual stress can be developed multiple times depending on the severity of the thermal brake load [29]. When the stresses developed in the material at the tread surface during the on-tread braking are below the yield limit, no plastic deformation occurs and develops no residual stress. When the stresses developed are higher than the yield strength, residual stress develops due to the plastic deformation. Since plastic deformation increases the yield strength of steel materials, the material at the tread surface has increased yield strength after thermal brake loading. The subsequent thermal brake loads accumulate no

plastic deformation and develop no residual stress as long as the compressive hoop stress developed in the material at the tread surface is below the new enhanced yield strength. This behavior is referred to as shakedown. However, the yield strength of the material can be enhanced only up to the shakedown limit. When the stresses exceed the shakedown limit, plastic deformation occurs with each subsequent brake loading. This excessive deformation in the material at the tread surface develops surface cracks and leads to ratcheting [30].

3.2 Previous studies

In the literature, considerable research has been performed to estimate residual stresses developed during the manufacturing process [27,29,31,32]. A few studies have also estimated the service-induced residual stresses [28,29,32]. A brief description of some studies is given below.

Dedmon et al. [31] estimated the residual stress developed in freight car locomotive wheel rims during the manufacturing process by performing decoupled thermal-structural analyses using a two-dimensional finite element model. The analyses were performed using the modified ANSYS that was specially designed to include a custom built creep model. The outer rim portion was divided into six different regions in an ‘onion skin’ pattern and these regions were modeled with different material properties. The maximum compressive hoop stress in the rim was estimated to as -87.9 ksi (-606 MPa).

Gordon et al. [27,29] estimated the as-manufactured residual stress in the passenger car wheel rim by performing decoupled thermal-structural finite element analyses using a two-dimensional model. The maximum compressive hoop stress developed in the rim was estimated to as -29 ksi (-200 MPa) and the depth of the compressive hoop stress layer below the tread surface was estimated to as 1.48 in (37.5 mm).

Wang and Pilon [32] estimated the residual stresses developed in freight car wheel rims during both the manufacturing process and under service conditions by performing decoupled thermal-structural analyses using a two-dimensional model. The as-manufactured residual stress distribution was estimated under two different types of heat treatment techniques: ideal and non-ideal. The results showed that the maximum compressive hoop stress developed during both types of heat treatment processes were about the same and were approximately -26.1 ksi (-180 MPa). The thermal brake loading under service conditions was simulated assuming a thermal brake load of 45 HP and the braking duration required for stress reversal in the material at the tread surface was estimated to as 57 minutes assuming the thermal brake load as 45 HP.

Gordon et al. [28,29] estimated the residual stress developed in passenger car wheels under service conditions by performing decoupled thermal-structural analyses using a two-dimensional finite element model. The results showed that the residual stress in the material at the tread surface reverses from compression to tension during the thermal brake loading under service conditions. The maximum tensile residual hoop stress developed in the material at the tread surface was estimated to as 51 ksi (350 MPa) and

the depth of the tensile hoop stress below the taping line was estimated to as 0.24 in (6 mm).

Liu et al. [33] performed a study to compare the residual stresses estimated from two-dimensional and three-dimensional finite element analyses in passenger car wheels. The residual stresses developed during both the manufacturing process and under service conditions were estimated. The rim portion of the three-dimensional model was meshed using much finer mesh compared to the other regions in order to accurately capture the contact stresses. The results indicated that the residual stress values estimated from both two-and three-dimensional models were in good agreement.

Most of the previous studies described above have estimated the residual stress distribution using a two-dimensional finite element model. In this Chapter, the residual stresses in a wheel are estimated using three-dimensional decoupled thermal-structural finite element analyses. To simulate the manufacturing process, thermal analysis is performed with convection boundary conditions on the wheel surfaces. The temperature distributions obtained from this thermal analysis are applied as thermal loads for structural analysis. The results represent as-manufactured residual stresses. To simulate the thermal brake loading under service conditions, thermal analysis is performed using a heat flux boundary condition on the tread surface. Structural analysis is performed, including the estimated as-manufactured residual stress as initial stress, and using the temperature distributions obtained from thermal analysis of the on-tread braking. The resultant stresses represent the complex combination of residual stresses developed

during both the manufacturing process and on-tread braking. The computed results are compared with the experimental data obtained at Transportation Technology Center, Inc., and the values reported in the literature. The three-dimensional residual stress distribution estimated in this Chapter will be useful in including residual stresses as initial stresses for 3D rolling contact analysis.

3.3 Methodology

Two sets of analyses are performed. In the first set, the manufacturing process is simulated and in the second set, the thermal brake loading under service conditions is simulated.

Figure 9 shows a three-dimensional finite element model of a 36" curved plate freight car wheel with a rim thickness of 1.5 in (38.1 mm) built in ANSYS [18]. The finite element model is built using SOLID70 elements, which have 8 nodes with temperature as the only degree of freedom, for the thermal analysis, and using SOLID185 elements, which have 8 nodes with three translational degrees of freedom, for the structural analysis. The finite element model contains 54,982 nodes and 48,224 elements. This finite element model is constructed using cylindrical co-ordinate system, with X-axis along the radial direction, Y-axis along the axial direction, and Z-axis along the circumferential direction.

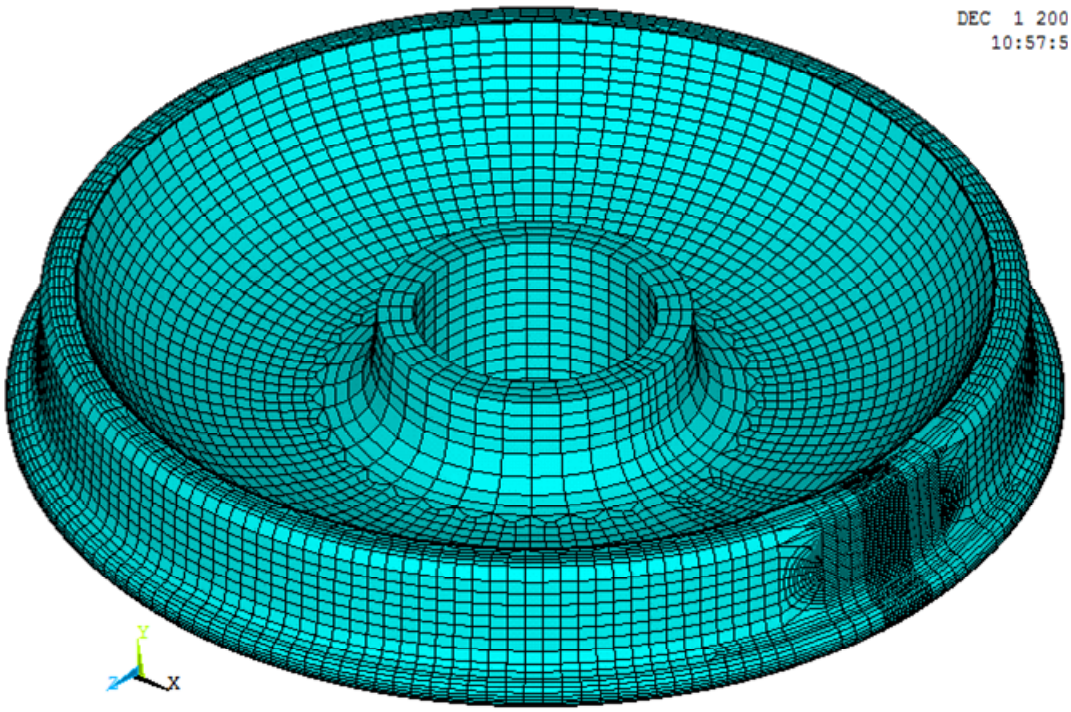

Figure 9 Finite element model of a railroad freight car wheel

3.3.1 Manufacturing Process

The wheel manufacturing process is simulated using two steps: non-linear transient thermal analysis and non-linear elastic-plastic structural analysis including creep effects. The thermal and structural analyses are performed using the same finite element model meshed with different types of elements. The analyses considered temperature dependent material properties.

In the non-linear transient thermal analysis, various steps of the manufacturing process are simulated using different convection boundary conditions on the wheel surfaces. The water spray rim quenching on the tread surface is simulated by applying a convection boundary condition on the tread surface with wheel-to-water heat transfer coefficient and

free convection boundary conditions on the remaining wheel surfaces. This thermal analysis estimates the temperature distributions in the wheel at various time steps.

The temperature distributions obtained from the thermal analysis are input as loads for non-linear elastic-plastic structural analysis including creep effects. Elastic-plastic analysis is performed as the material in the inner rim portion and plate yields in compression during rim quenching. The elastic-plastic effects are considered by using a bilinear isotropic hardening model [31]. The annealing of a stressed wheel at high temperature for long hours leads to stress relaxation; therefore, creep effects are included in the structural analysis using the Norton creep model [34]. This creep model expresses the creep strain rate as a function of the local temperature and effective stress as shown in Eq. (8).

$$\dot{\varepsilon}_{cr} = C_1 \sigma^{C_2} e^{-\left(\frac{C_3}{T}\right)} \tag{8}$$

where $\dot{\varepsilon}_{cr}$ is the creep strain rate; σ is the local effective stress; and T is the local temperature. C_1, C_2, and C_3 are constants. The resultant stresses of this structural analysis represent the as-manufactured residual stresses.

3.3.2 On-tread Braking

The thermal brake loading under service conditions is simulated using decoupled thermal-structural analyses, which include a non-linear transient thermal analysis and a non-linear elastic-plastic structural analysis. The same finite element model used for simulating the manufacturing process is used for on-tread braking simulation with

different boundary conditions. Temperature dependent material properties are considered for the analyses.

The thermal analysis of on-tread braking is divided into two steps. In the first step, the material at the tread surface is heated due to the frictional heat energy generated during the brake loading. This step is simulated using a heat flux boundary condition on the tread surface and free convection boundary conditions on all the wheel surfaces. In the second step, the entire wheel is allowed to cool down. This step is simulated by applying free convection boundary conditions on all the wheel surfaces. This thermal analysis estimates the temperature distributions in the wheel at various time steps.

The temperature distributions obtained from the thermal analysis of on-tread braking analysis are input as loads for non-linear elastic-plastic structural analysis. Elastic-plastic analysis is performed as the material at the tread surface yields in compression during the on-tread braking. The elastic-plastic effects are considered by using a bilinear isotropic hardening model [31]. The estimated as-manufactured residual stress distribution is included as initial stress for structural analysis of on-tread braking. The results of this structural analysis represent the residual stresses developed in the wheel due to both the manufacturing process and the thermal brake loading under service conditions.

3.4. Finite Element Analyses Details

3.4.1 Manufacturing Process

Table 2 shows the details of convection boundary conditions considered in the thermal analysis to simulate the manufacturing process [29].

Table 2 Convection boundary condition details (manufacturing process)

Process	Duration	Heat transfer coefficient				Ambient temperature	
		Wheel tread surface		Other wheel surfaces			
		Btu/s.in^2.°F	W/mm^2.°C	Btu/s.in^2.°F	W/mm^2.°C	°F	°C
Pre-quenching	90 s	9.51E-06	2.80E-05	9.51E-06	2.80E-05	77	25
Quenching	5 min	1.04E-03	3.07E-03	9.51E-06	2.80E-05	77	25
Pre-tempering	15 min	9.51E-06	2.80E-05	9.51E-06	2.80E-05	77	25
Tempering	4 h	9.51E-06	2.80E-05	9.51E-06	2.80E-05	860	460
Post-tempering	6 h	9.51E-06	2.80E-05	9.51E-06	2.80E-05	77	25

Table 3 shows the temperature dependent thermal material properties considered for the thermal analysis of the manufacturing process [29].

Table 3 Thermal material properties (manufacturing process)

Temperature		Thermal conductivity		Specific heat	
(°F)	(°C)	Btu/(s.in.°F)	W/(mm.°C)	Btu/(lbm.°F)	J/(kg.°C)
32	0	7.99E-04	5.97E-02	0.1002	419.49
662	350	5.47E-04	4.09E-02	0.1503	629.48
1297	703	4.04E-04	3.02E-02	0.1778	744.48
1299	704	4.04E-04	3.02E-02	0.1559	652.88
1310	710	4.01E-04	3.00E-02	0.1560	653.18
1472	800	3.34E-04	2.50E-02	0.1571	657.68
1742	950	3.62E-04	2.71E-02	0.1589	665.18
2192	1200	4.07E-04	3.05E-02	0.1618	677.28

For the structural analysis, constants of the Norton creep equation are assumed as C_1 = $4.64*10^{-8}$; C_2 = 12.5; and C_3 = 53712. Tables 4 and 5 list the temperature dependent mechanical material properties considered for the structural analysis.

Table 4 Mechanical material properties (manufacturing process)

Temperature		Young's modulus		Poisson's ratio	Expansion coefficient	
°F	°C	ksi	MPa		/°F	/°C
75	24	3.00E+04	2.07E+05	0.295	5.49E-06	9.89E-06
700	371	2.52E+04	1.74E+05	0.315	6.21E-06	1.12E-05
800	427	2.47E+04	1.70E+05	0.318	6.25E-06	1.12E-05
1000	538	2.37E+04	1.63E+05	0.324	6.28E-06	1.13E-05
1200	649	1.61E+04	1.11E+05	0.331	6.28E-06	1.13E-05
1350	732	1.02E+04	7.03E+04	0.336	6.26E-06	1.13E-05
1500	816	8.60E+03	5.93E+04	0.340	6.25E-06	1.13E-05
1600	871	8.00E+03	5.52E+04	0.343	6.25E-06	1.13E-05
1700	927	8.00E+03	5.52E+04	0.347	6.25E-06	1.13E-05
1800	982	6.70E+03	4.62E+04	0.350	6.26E-06	1.13E-05
1900	1038	4.00E+03	2.76E+04	0.353	6.26E-06	1.13E-05
2000	1093	3.60E+03	2.48E+04	0.356	6.26E-06	1.13E-05

Table 5 Plasticity material properties (manufacturing process)

Temperature		Yield strength		Tangent modulus	
°F	°C	ksi	MPa	ksi	MPa
75	24	113.00	779.11	3.00E+03	2.07E+04
700	371	112.20	773.59	2.52E+03	1.74E+04
800	427	83.20	573.64	2.47E+03	1.70E+04
1000	538	46.30	319.23	2.37E+03	1.63E+04
1350	732	8.40	57.92	1.02E+03	7.03E+03
1600	871	4.50	31.03	8.00E+02	5.52E+03

3.4.2 Thermal Brake Loading

The Association of American Railroad (AAR) Manual of Standards and Recommended Practices specifies the details of thermal and mechanical loads that need to be considered for locomotive and freight car wheel designs. According to AAR standards, specification S-660, the thermal brake loading needs to be considered by applying the thermal load uniformly on the tread surface area spanning over a distance of $3\frac{3}{8}$ in (85.725 mm) axi-symmetrically, centered along the line located at $3\frac{7}{16}$ in (87.3125 mm) from the back face of the wheel rim. According to AAR S-660, for a freight car wheel with diameter 36" and loading condition of 100-ton (263K Gross Rail Load), the braking conditions can be simulated by applying 35 HP thermal load on the wheel tread surface for 20 min [35].

This Chapter investigates the effects of thermal brake loading duration on the residual stress developed in the material at the tread surface during the manufacturing process. Six sets of analyses are performed with thermal brake loads of 35 HP and 45 HP for braking durations of 20 min, 40 min, and 60 min. The thermal brake load and the duration required for stress reversal on the tread surface are estimated.

In the thermal analysis, the on-tread braking simulation is divided into two steps. In the first step, the wheel tread surface is heated due to the thermal load input over braking duration. This step is simulated using a heat flux boundary condition on the specified tread surface area and convection boundary conditions, assuming the heat transfer coefficient as $2.84*10^{-5}$ W/mm^2.°C ($9.64*10^{-6}$ Btu/s.in^2.°F) and the ambient temperature

as 21 °C (70 °F), on the remaining wheel surface areas. In the second step, the entire wheel is allowed to cool down for 10 hours. This step is simulated using free convection boundary conditions, assuming the heat transfer coefficient as $2.84*10^{-5}$ W/mm^2.°C ($9.64*10^{-6}$ Btu/s.in^2.°F) and the ambient temperature as 21 °C (70 °F), on all wheel surface areas.

The heat treated material properties of class *C* wheel steel reported in the literature are considered for simulating the thermal brake loading under service conditions [32]. Table 6 lists the temperature dependent thermal material properties considered for thermal analysis of the on-tread braking.

Table 6 Thermal material properties (on-tread braking)

Temperature		Thermal conductivity		Specific heat	
(°F)	(°C)	Btu/(s.in.°F)	W/(mm.°C)	Btu/(lbm.°F)	J/(kg.°C)
70	21	5.05E-04	3.78E-02	0.11892	497.89
100	38	5.10E-04	3.81E-02	0.11992	502.08
200	93	5.26E-04	3.93E-02	0.12380	518.33
300	149	5.38E-04	4.02E-02	0.12846	537.84
400	204	5.45E-04	4.07E-02	0.13399	560.99
500	260	5.49E-04	4.10E-02	0.14030	587.41
600	316	5.48E-04	4.10E-02	0.14743	617.26
700	371	5.44E-04	4.07E-02	0.15557	651.34
800	427	5.35E-04	4.00E-02	0.16413	687.18
900	482	5.23E-04	3.91E-02	0.17369	727.21
1000	538	5.06E-04	3.78E-02	0.18407	770.66
1100	593	4.85E-04	3.63E-02	0.19525	817.47
1200	649	4.60E-04	3.44E-02	0.20725	867.71
1300	704	4.31E-04	3.22E-02	0.22007	921.39
1400	760	3.99E-04	2.98E-02	0.19521	817.31
1500	816	3.62E-04	2.71E-02	0.16439	688.27
1600	871	3.41E-04	2.55E-02	0.16010	670.31

The time dependent Young's modulus values and creep model parameters used in simulating the manufacturing process are also used in simulating the on-tread braking. Tables 7 and 8 list the mechanical properties considered for the structural analysis of the on-tread braking.

Table 7 Plasticity material properties (on-tread braking)

Temperature		Yield strength		Tangent modulus	
°F	°C	ksi	MPa	ksi	MPa
70	21	110.3	760.7	1770.8	1.22E+04
400	204	100.0	689.8	2218.9	1.53E+04
800	427	80.4	554.6	1524.4	1.05E+04
1000	538	47.7	328.7	214.0	1.48E+03
1200	649	16.2	111.4	56.0	3.86E+02
1500	816	5.0	34.5	43.8	3.02E+02

Table 8 Mechanical material properties (on-tread braking)

Temperature		Density		Expansion coefficient	
°F	°C	lbm/in^3	kg/mm^3	/°F	/°C
70	21	0.28166	7.80E-06	5.12E-06	9.22E-06
100	38	0.28155	7.79E-06	5.28E-06	9.51E-06
200	93	0.28105	7.78E-06	5.76E-06	1.04E-05
300	149	0.28045	7.76E-06	6.18E-06	1.11E-05
400	204	0.27987	7.75E-06	6.64E-06	1.19E-05
500	260	0.27921	7.73E-06	6.84E-06	1.23E-05
600	316	0.27852	7.71E-06	7.09E-06	1.28E-05
700	371	0.27782	7.69E-06	7.31E-06	1.31E-05
800	427	0.27709	7.67E-06	7.48E-06	1.35E-05
900	482	0.27637	7.65E-06	7.62E-06	1.37E-05
1000	538	0.27570	7.63E-06	7.73E-06	1.39E-05
1100	593	0.27400	7.58E-06	7.82E-06	1.41E-05
1200	649	0.27429	7.59E-06	7.88E-06	1.42E-05
1300	704	0.27357	7.57E-06	7.94E-06	1.43E-05
1400	760	0.27413	7.59E-06	7.99E-06	1.44E-05
1500	816	0.27305	7.56E-06	8.03E-06	1.45E-05
1600	871	0.27214	7.53E-06	-	-

3.5 Wheel Wear

Wheel wear, the process of surface material removal under service conditions, reduces the rim thickness and alters the tread profile. Since the contact stress in a wheel rim depends on the rim thickness and the tread profile, it is important to consider wheel wear. The two dominant types of wear in railroad wheels are adhesive wear and delamination wear. Adhesive wear occurs when thin flakes that are formed on the wheel surface adhere to the asperities on the rail and break off from the wheel. This type of wear is relatively mild and the debris consists of iron oxides and metallic iron. Delamination wear occurs when a surface crack kinks and propagates into the wheel surface and breaks off a piece from the wheel. This type of wear is very severe compared to the adhesive wear [30].

The wear models available in the literature can be classified into two types: energy transfer models and sliding wear models. Energy transfer models estimate the wheel wear (loss of surface material) as a function of energy dissipated in the contact patch. Sliding wear models estimate the wheel wear as a function of material hardness, sliding distance and the normal force [36]. The Archard wear model is one of the most well-known wear models used to estimate the wear due to rolling contact loading [37]. This model relates the wear volume to the normal and tangential forces, material properties, and sliding distance.

Since it is computationally expensive to update the wheel profile considering wheel wear after each cycle, this research assumes uniform wheel wear for the sake of illustration. The geometry of the thinner rim thickness wheel is obtained by imposing the tread

surface at the required rim thickness. The methodology developed in this research to estimate residual stresses in a thinner rim wheel can be applied considering any other wear model.

Since wheel wear removes the surface material, thereby removing the residual stresses in the outer strip, the residual stresses in a thinner rim wheel are significantly different from those in a new wheel. This Chapter develops a methodology to estimated residual stresses in a thinner rim wheel. The as-manufactured residual stress component in a thinner rim wheel is estimated using decoupled thermal-structural analyses and sub-modeling concepts. The new wheel geometry is considered as the full model and the thinner rim wheel geometry is considered as the sub-model. The transient thermal analysis is performed using the full model to estimate the temperatures in the wheel during the wheel. The temperatures obtained from the full model are applied to the sub-model as inputs and non-linear elastic-plastic structural analysis is performed to estimate the as-manufactured residual stress component in a thinner rim thickness wheel. The methodology to estimate service-induced residual stresses in a thinner rim wheel is similar to that of the new wheel. The service-induced residual stresses in a thinner rim are estimated considering the estimated as-manufactured residual stress component as initial stress.

3.6 Results and Discussion

3.6.1 As-manufactured residual stresses

Railroad freight car wheels with a diameter of 36 in and rim thicknesses of 1.5 in and 0.875 in are considered in this Chapter. A wheel with a rim thickness of 1.5 in represents a new wheel, and with a rim thickness of 0.875 in represents a thinner rim thickness wheel. Figure 10 shows the estimated as-manufactured residual stresses in a new wheel. Figure 11 shows the estimated as-manufactured residual stress components in a thinner rim thickness wheel.

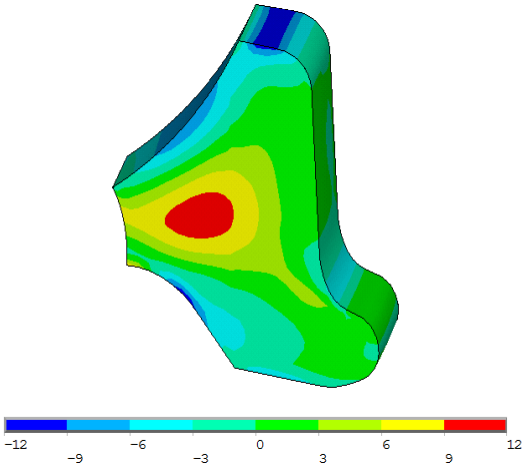

(a) Radial stress

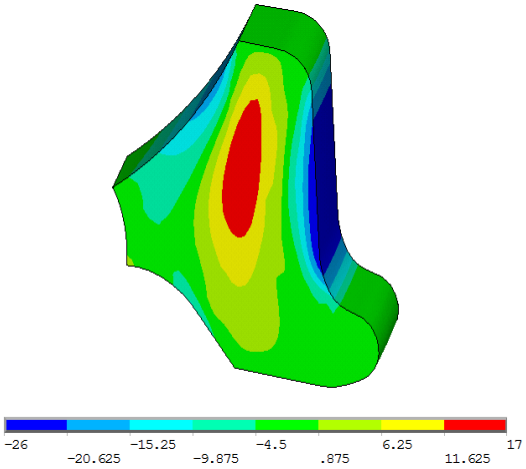

(b) Axial stress

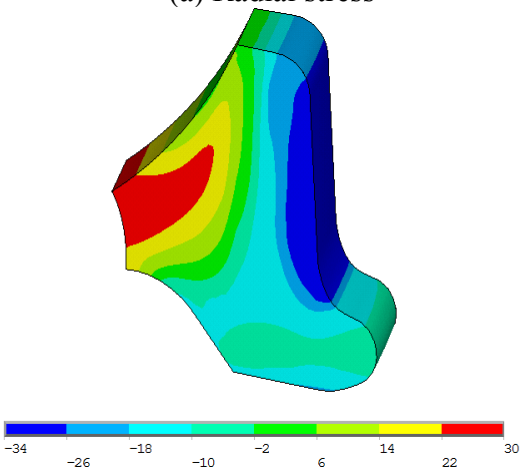

(c) Hoop stress

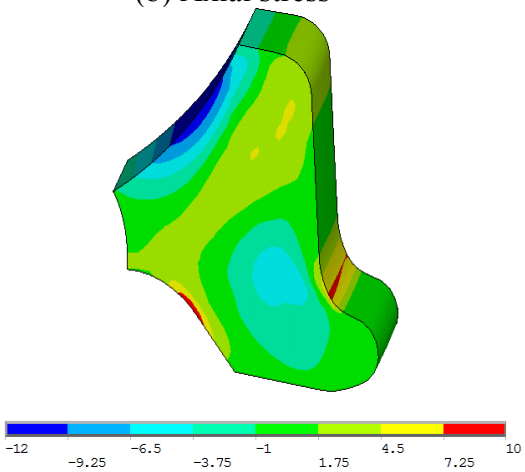

(d) Shear stress

Figure 10 Estimated as-manufactured residual stresses in a new wheel.

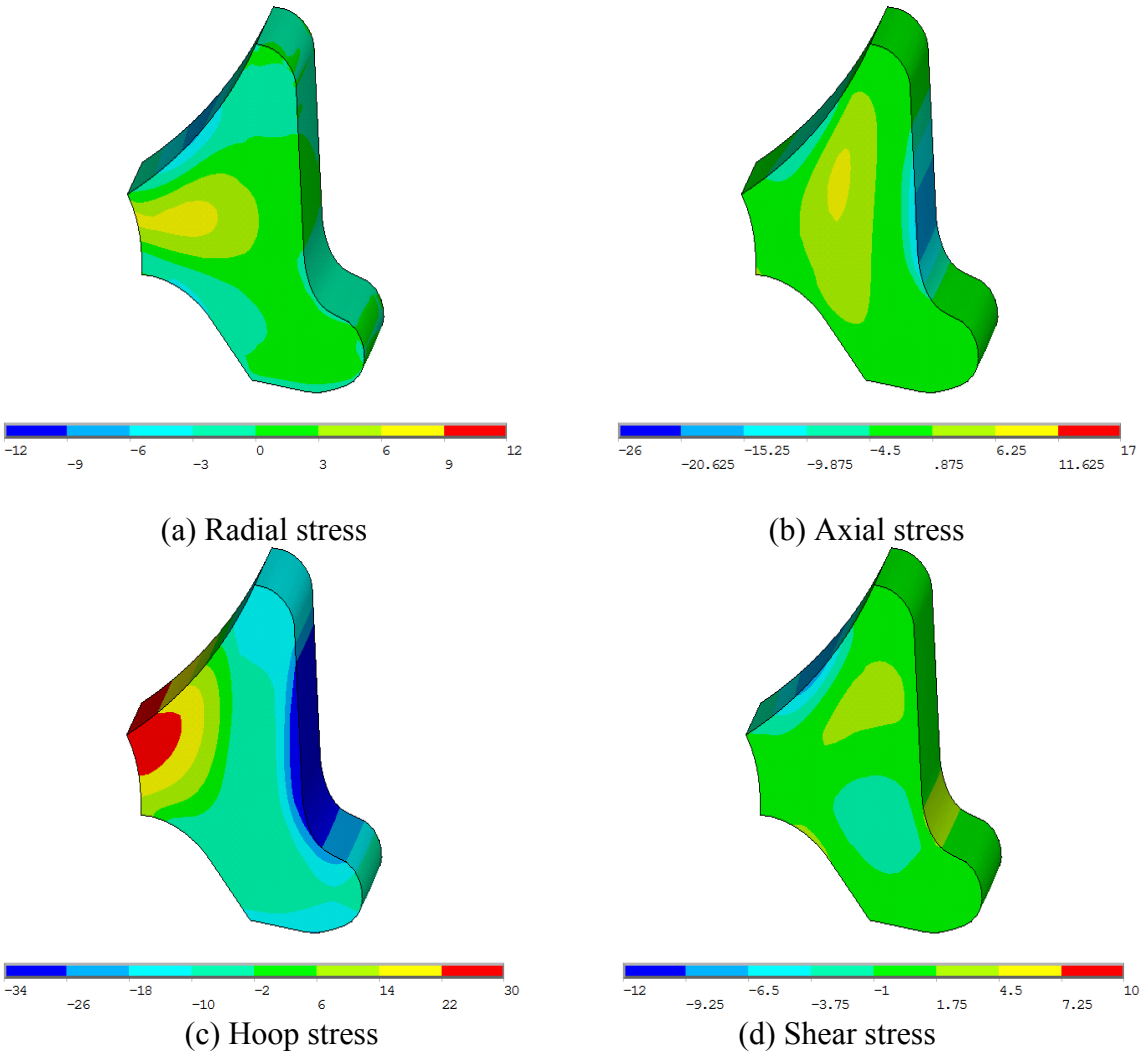

(a) Radial stress

(b) Axial stress

(c) Hoop stress

(d) Shear stress

Figure 11 Estimated as-manufactured residual stress in a thinner rim wheel.

The simulation results show that compressive hoop stress is developed in the new wheel rim. The radial stress along the tread surface is close to zero as it is a free surface. The maximum compressive axial stress is developed along the taping line in the wheel rim and is equal to -23.6 ksi (-162.7 MPa). The maximum compressive hoop stress is developed along the taping line in the wheel rim and is equal to -35.75 ksi (-246.5 MPa), and the depth of the compressive hoop stress layer below the taping line is 1.1 in (28 mm).

In the literature, Gordon et al. [27,29] estimated the compressive residual hoop stress on the taping line as -29 ksi (-200 MPa) and the depth of the compressive hoop stress layer below the taping line as 1.42 in (36 mm) for passenger car wheels. This matches well with the computed results and verifies our model, accounting for differences in wheel geometry, temperature variations, and material properties. The authors believe that the manufacturing processes for both passenger and freight car wheels are similar and therefore the residual stresses developed during the manufacturing process in both type of wheels are of similar magnitude.

Figure 12 shows the as-manufactured residual hoop stresses measured in new wheel rims at Transportation Technology Center, Inc. (TTCI) [38] and the computed results. The seven wheels considered for this experimental study were manufactured by different wheel manufacturing companies in North America. The residual hoop stresses are measured at three different locations in the rims: front rim face; taping line; and flange using saw cut displacement method. The residual strains at these three locations are measured using the strain gauges and the corresponding residual stresses are estimated using the mechanical properties of the specific wheel. The material composition and mechanical properties of the wheels are proprietary information and only masked data are given here. Figure 12 shows that the measured residual stresses vary from -80 ksi (-552 MPa) to -5 ksi (-34.5 MPa). This high variation is due to different heat treatment techniques used by different wheel manufacturing companies. The computed residual stresses from our analysis at the front rim face, taping line, and flange are -25.2 ksi (-

173.7 MPa), -35.75 ksi (-246.5 MPa), and -27.8 ksi (-191.7 MPa). The computed residual stresses are within the experimental data range, and are relatively closer to that of the wheel numbered 4; the observed difference is about 10%. This validates the computed results of this study.

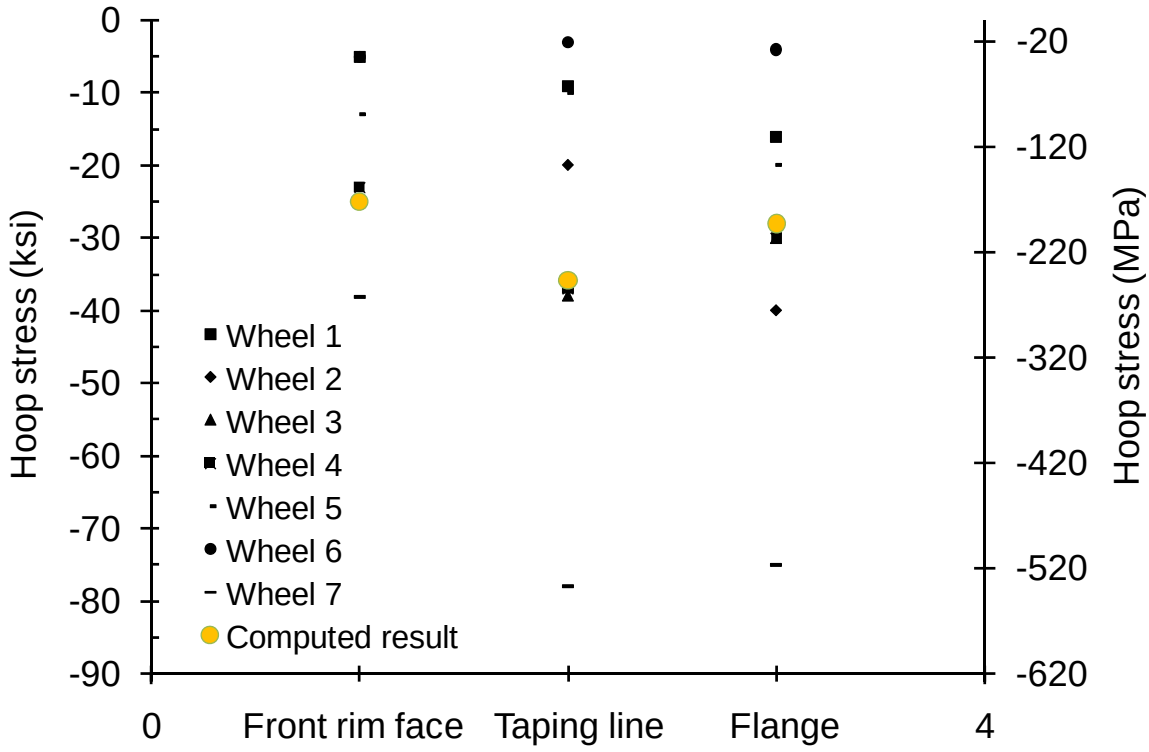

Figure 12 Validation of the computed results using experimental data.

Using two-dimensional finite element analysis, Gordon et al. [27,29], Wang and Pilon [32], and Dedmon et al. [31] have previously estimated the maximum compressive residual hoop stresses developed during the manufacturing process in the wheel rim as -29 ksi (-200 MPa), -26 ksi (-180 MPa), and -87.9 ksi (-606 MPa) respectively. This Chapter estimated this stress as -33.75 ksi (-246.5 MPa). The computed results are in

relatively good agreement with that of the Gordon et al. and Wang and Pilon studies. The small difference observed could be due to the consideration of different material properties and different heat treatment techniques, such as quenching duration, temperature in the draw furnace, and so forth. The significant difference observed from that of the Dedmon et al. study is due to usage of different creep models.

3.6.2 Service-induced residual stress

Six sets of analyses are performed considering thermal brake loads of 35 HP and 45 HP for durations of 20 min, 40 min, and 60 min. The thermal brake loading under service conditions develops high temperatures in the wheel rim. The development of temperatures above the austentizing temperature under severe braking conditions leads to metallurgical transformation in the material at the tread surface to form martensite, which is a brittle material. This brittle material cracks under the rolling contact loading leading to wheel spalling [30].

Just for the sake of illustration, only the computed results with a thermal brake load of 45 HP and a braking duration of 60 min are shown in this Chapter out of the six set of analyses. Figures 13 and 14 show the estimated service-induced residual stresses in a new wheel and in a thinner rim thickness wheel respectively.

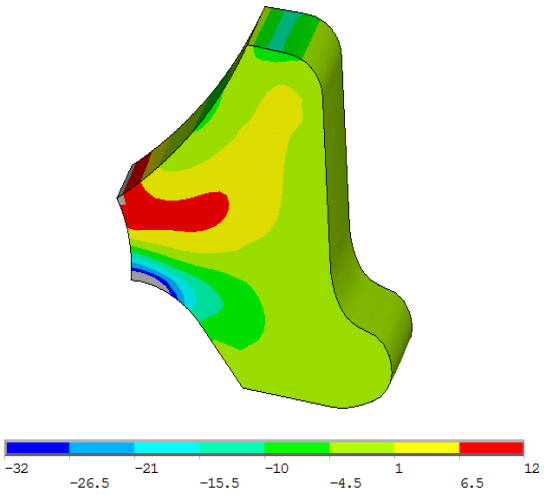

(a) Radial stress

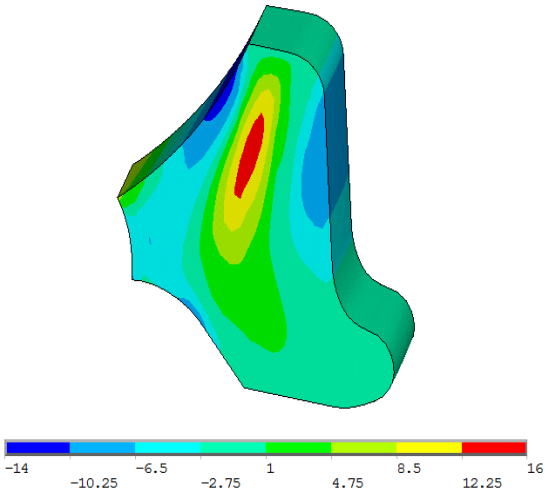

(b) Axial stress

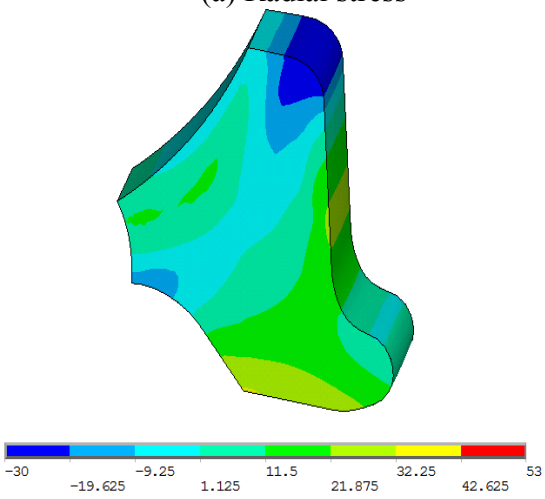

(c) Hoop stress

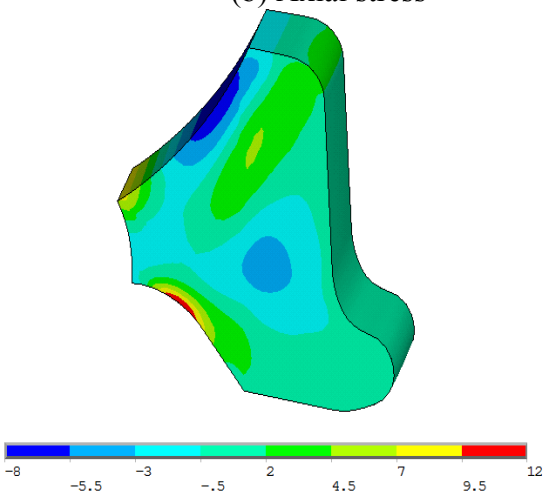

(d) Shear stress

Figure 13 Estimated service-induced residual stresses in a new wheel.

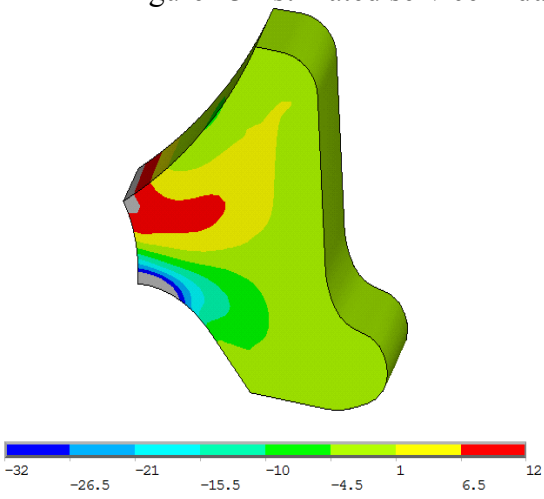

(a) Radial stress

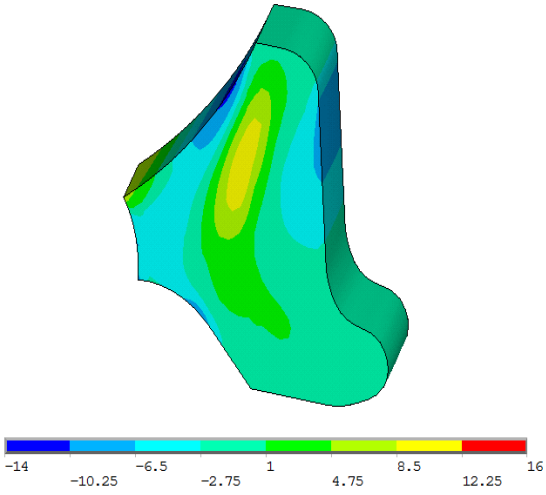

(b) Axial stress

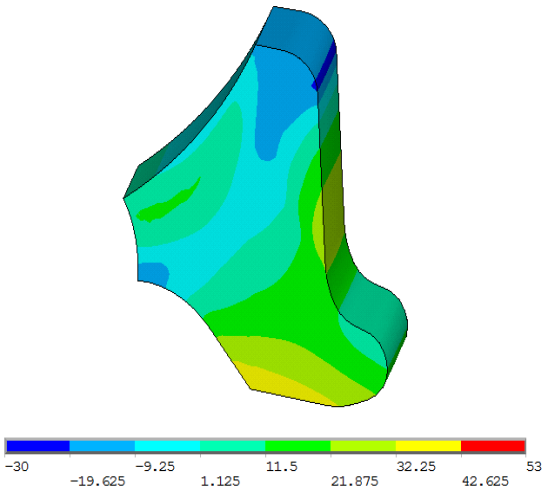

(c) Hoop stress

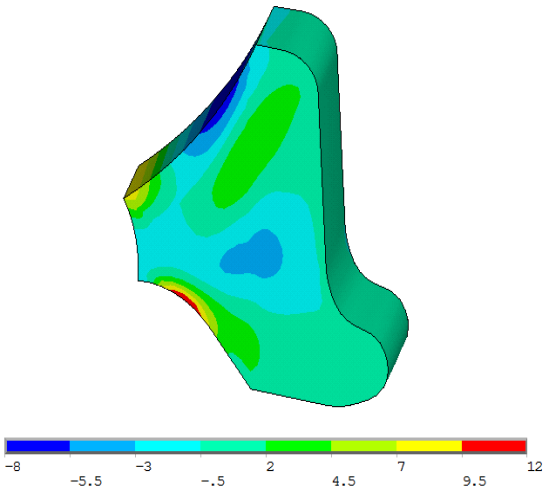

(d) Shear stress

Figure 14 Estimated service-induced residual stresses in a thinner rim thickness wheel.

The results show that the residual hoop stress along the taping line due to a thermal brake load of 45 HP for 60 min is 22 ksi (151.7 MPa) in a new wheel. This shows that detrimental residual hoop stress develops in the outer rim portion due to the thermal brake loading under service conditions.

Figure 15 shows the variation of service-induced residual hoop stress distributions below the taping line for braking durations 20 min, 40 min, and 60 min with a thermal load of 45 HP. The results show that the residual stress on the taping line is not reversed for braking durations of 20 min and 40 min with a thermal input of 45 HP. Only a thermal brake loading for 60 min with a thermal input of 45 HP develops tensile residual hoop stress on the taping line and the depth of the tensile residual hoop stress below the taping line is 0.30 in (7.5 mm). The results show that the approximate braking duration for stress reversal in the rim with a thermal load of 45 HP is approximately 50 min.

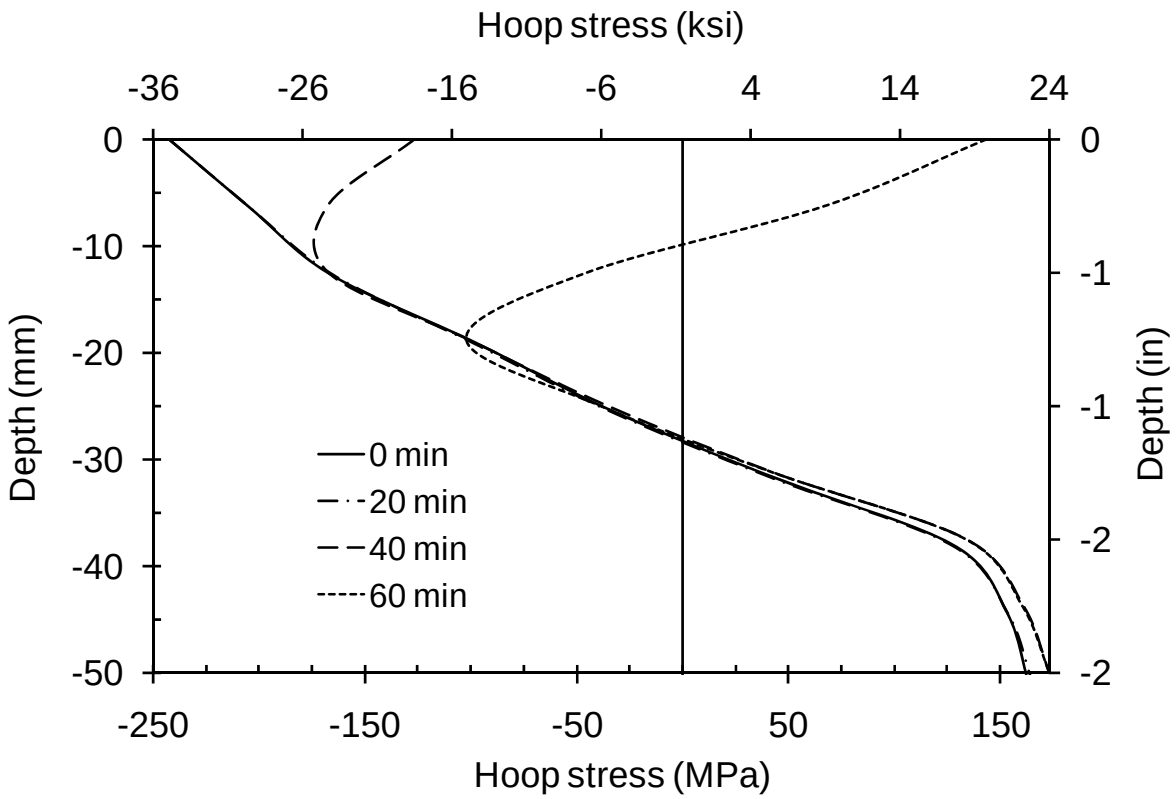

Figure 15 Variation of residual hoop stress below the taping line – thermal load of 45 HP.

In the literature, Gordon et al. [28,29] estimated the depth of the tensile residual hoop stress layer developed during the thermal brake loading under service conditions as 0.24 in (6 mm). The computed result is in good agreement with that of the Gordon et al. considering the differences in wheel geometry, applied load, and material properties.

3.7 Summary and Conclusions

The residual stresses developed in a railroad wheel during both the manufacturing process and under service conditions are estimated using three-dimensional, decoupled thermal-structural finite element analyses. The computed results are validated with the

experimental values and with those in the literature. The findings of this Chapter are summarized below:

1. The maximum compressive residual hoop stress developed in a new wheel rim during the manufacturing process is -35.75 ksi (-246.5 MPa) and the depth of the compressive stress layer below the tread surface is 1.25 in (31.75 mm).
2. The computed as-manufactured results are in good agreement with the experimental data obtained at the TTCI.
3. The temperatures developed in the wheel rims during the on-tread braking under service conditions depend on the magnitude of the thermal load and the braking duration.
4. On-tread braking with a thermal load of 45 HP for a braking duration of 60 min develops detrimental tensile residual hoop stress.
5. The maximum tensile hoop stress developed in a new wheel due to a thermal load of 45HP for 60 min is 22 ksi (151.7 MPa) and the depth of the tensile stress layer below the tread surface is about 0.4 in (10 mm).
6. The braking duration required for stress reversal in the wheel rim due to on-tread braking with a thermal load of 45 HP is 50 min.
7. The service-induced residual stresses in a thinner rim wheel are significantly different from those in a new wheel as the wheel wear removes the as-manufactured residual stress in the outer strip.

The three-dimensional residual stress distributions estimated in this Chapter will be included as initial stresses for rolling contact analysis of shattered rim and vertical split

rim cracking to simulate realistic service conditions. The effect of residual stresses and wheel wear on shattered rim and vertical split rim cracking will be investigated in the next Chapter.

CHAPTER 4

EFFECT OF VARIOUS PARAMETERS ON SUB-SURFACE CRACKING

4.1 Introduction

Shattered rim and vertical split rim cracking are considered in this research as these are the two most dominant failure types. Shattered rim cracks propagate at deeper depths below the tread surface approximately parallel to the tread surface. Vertical split rim cracks propagate at shallow depths below the tread surface, approximately parallel to the front rim face or back rim face. The sub-surface crack propagation rate depends on several parameters, such as wheel geometry (diameter, rim thickness, and plate design), loading conditions (magnitude and location), residual stresses in the rim due to the manufacturing process and the thermal brake loading under service conditions, wheel wear, and sub-surface crack attributes (size, shape, location, and orientation). This Chapter investigates the effect of some of these important parameters and the critical parameters that can trigger shattered rim or vertical split rim cracking are identified. The equivalent stress intensity factor range (ΔK_{eq}) at a sub-surface crack tip can be estimated using the methodology developed in the Chapter 2. Numerical studies are performed to estimate the ΔK_{eq} values at various sub-surface cracks considering different possible combination of input parameters. The calculated ΔK_{eq} values are used to investigate the effect of various parameters and to identify critical parameters that can trigger either a shattered rim or vertical split rim failure.

The wheel geometry (wheel diameter, plate design, and rim thickness) can affect the shattered rim and vertical split rim cracking. This Chapter considers a wheel diameter of 36 in and a curved plate freight car wheel. The Chapter focuses only on the rim thickness as this parameter is more significant compared to the other two parameters. Thinner rim thickness increases the contact stress, thereby decreases the wheel failure life. Hannah et al. [39] considered a simple roller and plate example and have shown that the contact stress increases with decrease in plate thickness. The condemning rim thickness limits according to Association of American Railroads (AAR) and Federal Railroad Administration (FRA) are 0.875 in and 0.6875 in respectively [40,41].

The loading attributes (magnitude and location) can affect the shattered rim and vertical split rim cracking. A railroad wheel can experience high wheel loads due to built up treads or due to wheel out-of-roundness caused by surface defects. A high wheel load increases the contact stresses and stresses in the wheel rim, thereby affecting the sub-surface cracking. The normal rail-wheel contact location is centered along the taping line. However, when the wheel travels over a curve or over diamond crossing points, the rail-wheel contact location can shift laterally. The lateral shift in the rail-wheel contact location shifts the applied wheel load location. The lateral shift in the load location can affect contact stresses and stresses in the wheel rim, thereby affecting the sub-surface cracking. This Chapter investigates the effect of load magnitude and location on sub-surface cracking.

The shattered rim and vertical split rim crack growth rates depend on crack size, crack orientation, crack lateral location, and crack vertical location below the tread surface. This Chapter investigates the effect of above parameters and identifies the critical crack depth and critical crack orientation for shattered rim and vertical split rim cracking. The effect of crack lateral location is also investigated.

4.2 Methodology

The effect of various parameters on sub-surface cracking is investigated using equivalent stress intensity factor ranges (ΔK_{eq}) at sub-surface crack tips obtained by performing numerical studies with various combinations of input parameters. The equivalent stress intensity factor range (ΔK_{eq}) at a sub-surface crack tip is estimated using three-dimensional, multi-resolution finite element analysis and a mixed-mode crack model based on critical plane concepts. The methodology for estimating ΔK_{eq} is detailed in Chapter 2. Parametric studies are performed to identify critical parameters for shattered rim and vertical split rim cracking.

4.3 Results and Discussion

4.3.1 Shattered rim cracking

Railroad freight car wheels with a nominal diameter of 36 in and rim thicknesses 1.5 in, 0.875 in, and 0.6875 in are considered. Since the rim thicknesses 0.875 in and 0.6875 in correspond to the Association of American Railroads (AAR) and the Federal Railroad Administration (FRA) condemning rim thickness limits respectively, these values are considered in this Chapter.

Full model analyses are performed using the methodology described in Chapter 2 to simulate three different initial residual stress states: (1) no residual stress, (2) as-manufactured residual stress, and (3) residual stresses developed due to both the manufacturing process and the on-tread braking for 60 min with a thermal load of 45 HP. From the results of Chapter 3, it is observed that the residual hoop stress along the taping line on the tread surface is -34 ksi for the as-manufactured residual stress case,and 32 ksi for the on-tread braking case.

This Chapter considers wheel loads ranging from 50 kips to 200 kips with an increment of 25 kips. Nominal wheel load for a 36 in diameter wheel is 35.75 kips. Wheels are condemnable under AAR rules at 90 kips impact load, but larger impact loads have been recorded. This Chapter considers cracks at various depths below the tread surface ranging from 1/8 in to 1 in with increments of 1/8 in.

The mechanical loads on the tread surface are applied over a Hertzian contact area centered along the taping line and shattered rim cracks are considered directly below the load location. The contact area parameters depend on the wheel geometry and load magnitude. Table 9 shows Hertzian contact parameters for various cases considered, where C_a is the semi-major axis of the elliptical contact area (along the track direction) and C_b is the semi-minor axis of the elliptical contact area (along the lateral direction).

Table 9 Hertzian contact parameters

Wheel load (kips)	C_a (semi-major axis) (in)	C_b (semi-minor axis) (in)
50	0.372	0.294
75	0.426	0.337
100	0.468	0.371
125	0.505	0.399
150	0.536	0.424
175	0.564	0.447
200	0.590	0.467

Figure 16 shows the stress results of the full model analysis performed under a wheel load of 150 kips. This full model analysis is performed including both as-manufactured and service-induced residual stresses. The stress contours for rim thicknesses 1.5 in, 0.875 in, and 0.6875 in are shown in the same order in Figure 16.

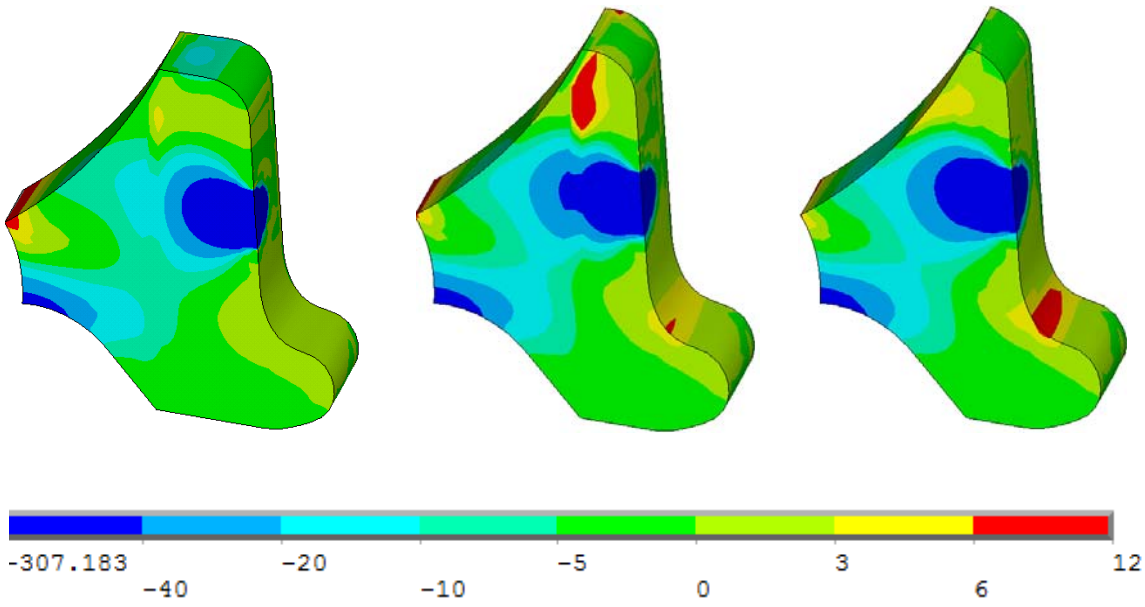

Figure 16(a) Radial stress (ksi) in wheel rims under a mechanical load of 150 kips (considering both as-manufactured and service-induced residual stresses).

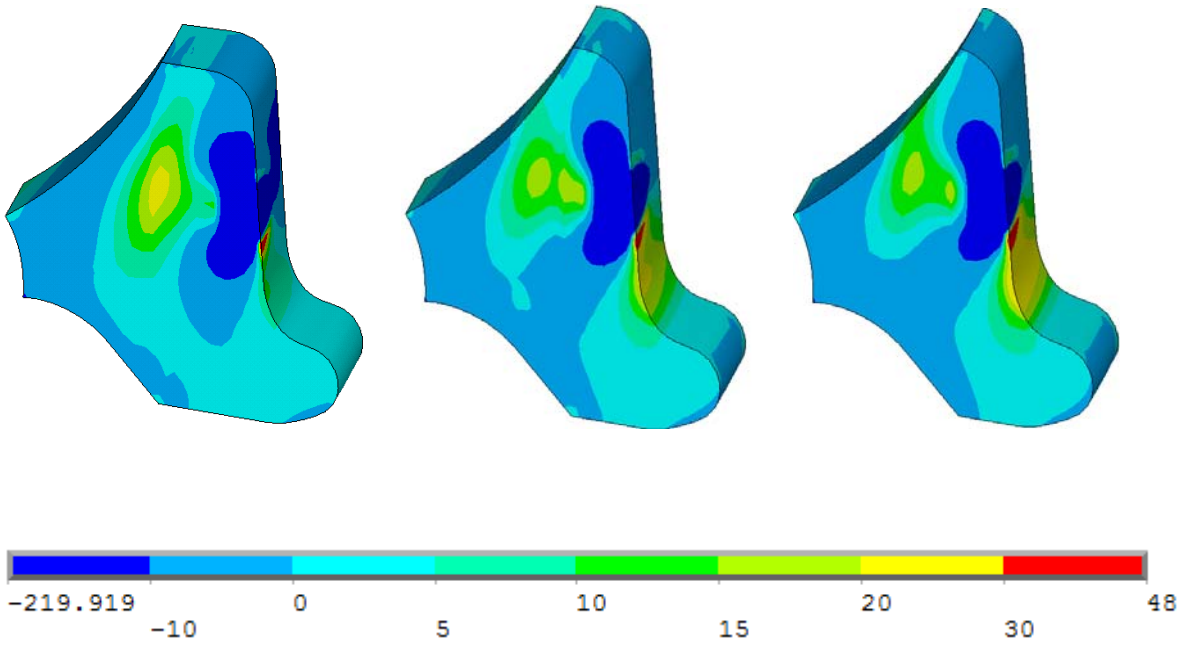

Figure 16(b) Axial stress (ksi) in wheel rims under a mechanical load of 150 kips (considering both as-manufactured and service-induced residual stresses).

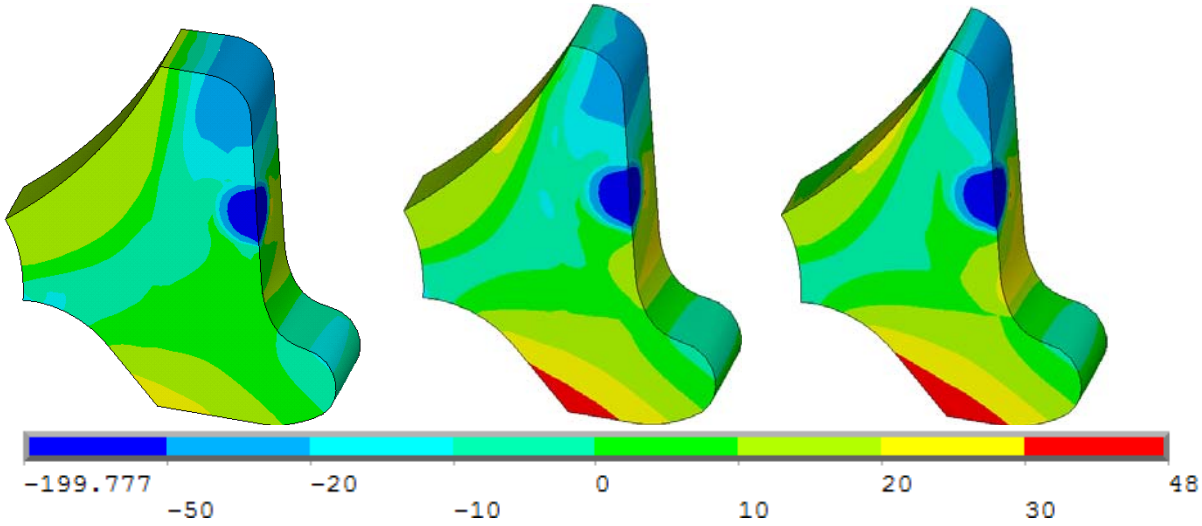

Figure 16(c) Hoop stress (ksi) in wheel rims under a mechanical load of 150 kips (considering both as-manufactured and service-induced residual stresses).

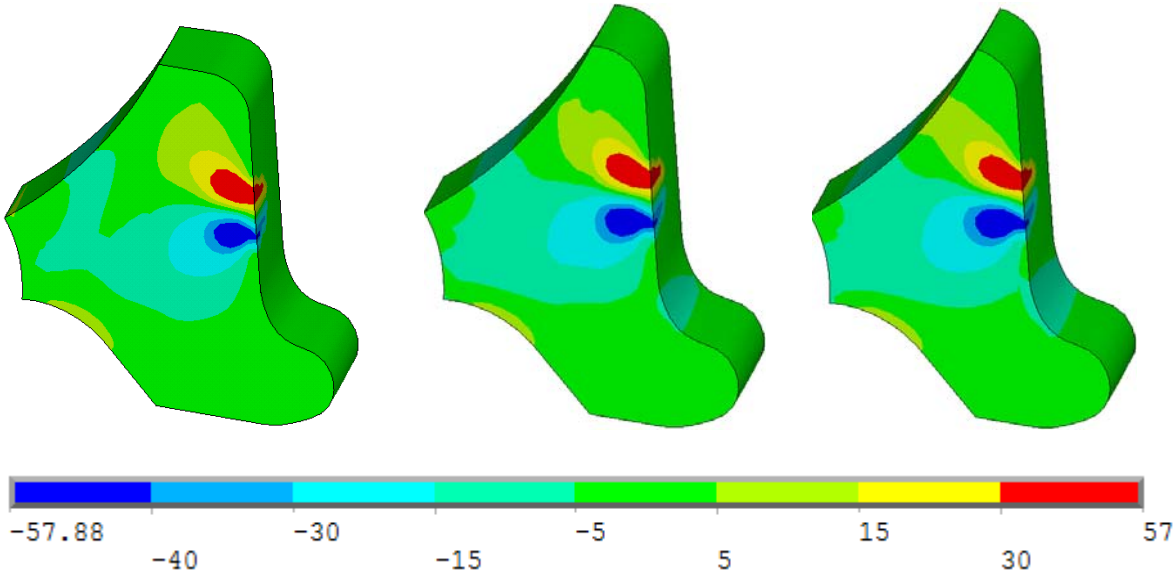

Figure 16(d) Shear stress - τ_{xy} (ksi) in wheel rims under a mechanical load of 150 kips (considering both as-manufactured and service-induced residual stresses).

The full model analyses are performed for various load magnitudes and only sample results for load magnitude 150 kips are shown in this Chapter. The results from the full model analyses are applied as boundary conditions to the sub-model to simulate shattered rim cracking. The methodology of full model analysis and sub-model analysis is detailed in Chapter 2.

This Chapter considers sub-surface shattered rim cracks of sizes 1 mm, 1.6 mm, 2.25 mm, and 3.175 mm at an orientation of 20° to the tread surface. The rationale in selecting these crack sizes is because 1 mm is the current practical limit of ultrasonic testing equipment, 1.6 mm represents the current AAR maximum allowable defect limit, and 2.25 mm and 3.175 mm represent historical AAR maximum allowable defect sizes. This research performed a few parametric studies and found that a crack orientation of 20° to

the tread surface is critical. This finding is in consistent with the values reported in the literature [20] and the field data observed at TTCI.

Figure 17 shows the variation of ΔK_{eq} at shattered rim crack tips with the rim thickness under a wheel load of 200 kips. The shattered rim crack is always considered directly below the load location (over a Hertzian contact area centered along the taping line). The results are shown for all considered crack sizes and crack depths.

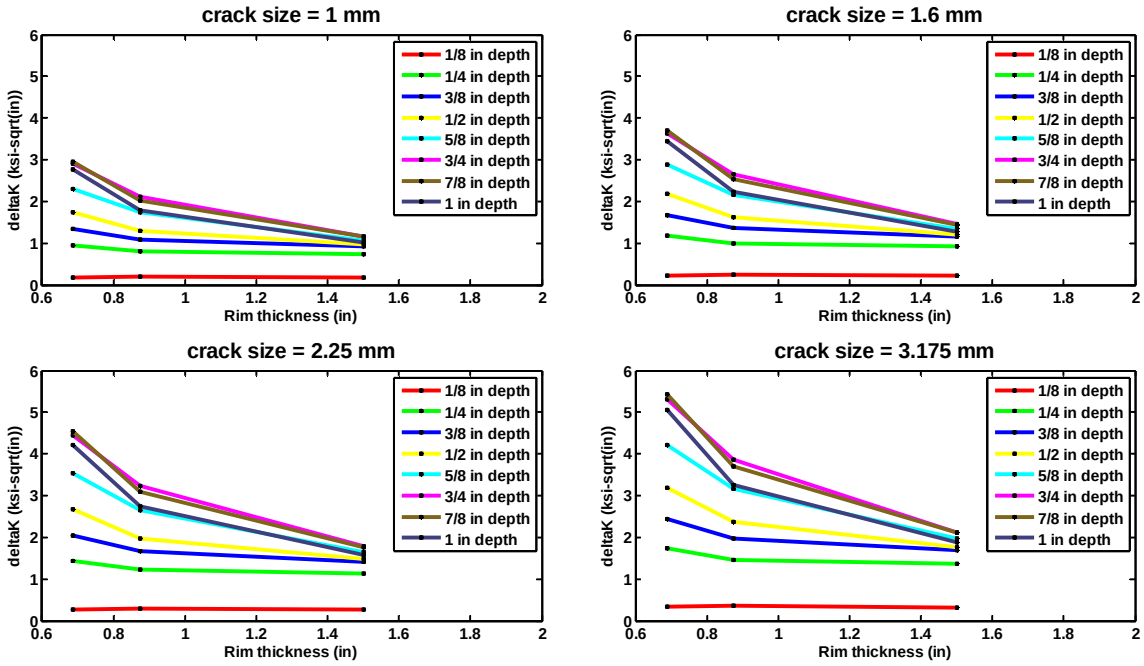

Figure 17 Variation of ΔK_{eq} (ksi-√in) at crack tips with rim thickness under a wheel load of 150 kips (considering both as-manufactured and service-induced residual stresses).

This Chapter performed an extensive parametric study, considering different load magnitudes (50 kips, 75 kips, 100 kips, 125 kips, 150 kips, 175 kips, and 200 kips), crack sizes (1 mm, 1.6 mm, 2.25 mm, and 3.175 mm), crack depths (1/8 in to 1 in with an

incremental depth of 1/8 in below the tread surface), rim thicknesses (1.5 in, 0.875 in, and 0.6875 in), and residual stress states (no residual stress state, as-manufactured residual stress state, and service-induced residual stress state). The sample results for some of the cases considered are only shown in this Chapter. Combination of above variables resulted in a total of 2016 simulations. The full model analyses provide the required boundary conditions to the sub-model analyses.

Figure 18 is an "effects plot" showing the overall relative effect of each parameter considered in this analysis. The data in this plot is generated by averaging the stress intensity factor results from all of the analyses in which one variable is held constant. For example, of the 2016 total analyses conducted, 504 were conducted with a crack size of 1 mm. Averaging the stress intensity factor results from these 504 analyses gives a result of 1.08 ksi-√in. Likewise, the average stress intensity factor from the 504 analyses with a crack size of 1.6 mm gives a result of 1.35 ksi√in. While this type of plot does not capture all of the interactions occurring between variables, it does give a broad view of the relative importance of each variable on shattered rim cracking.

The methodology developed in this Chapter can predict the conditions that can lead to shattered rim crack propagation by comparing the equivalent stress intensity factor range at the crack tip to the mode I threshold stress intensity factor range. The threshold stress intensity factor range depends on the material and the R-ratio (ratio of minimum stress to maximum stress). The magnitude of threshold stress intensity factor range will be lower

for higher R-ratios. The R-ratios will be very low for cases with high wheel loads and thinner rim thicknesses.

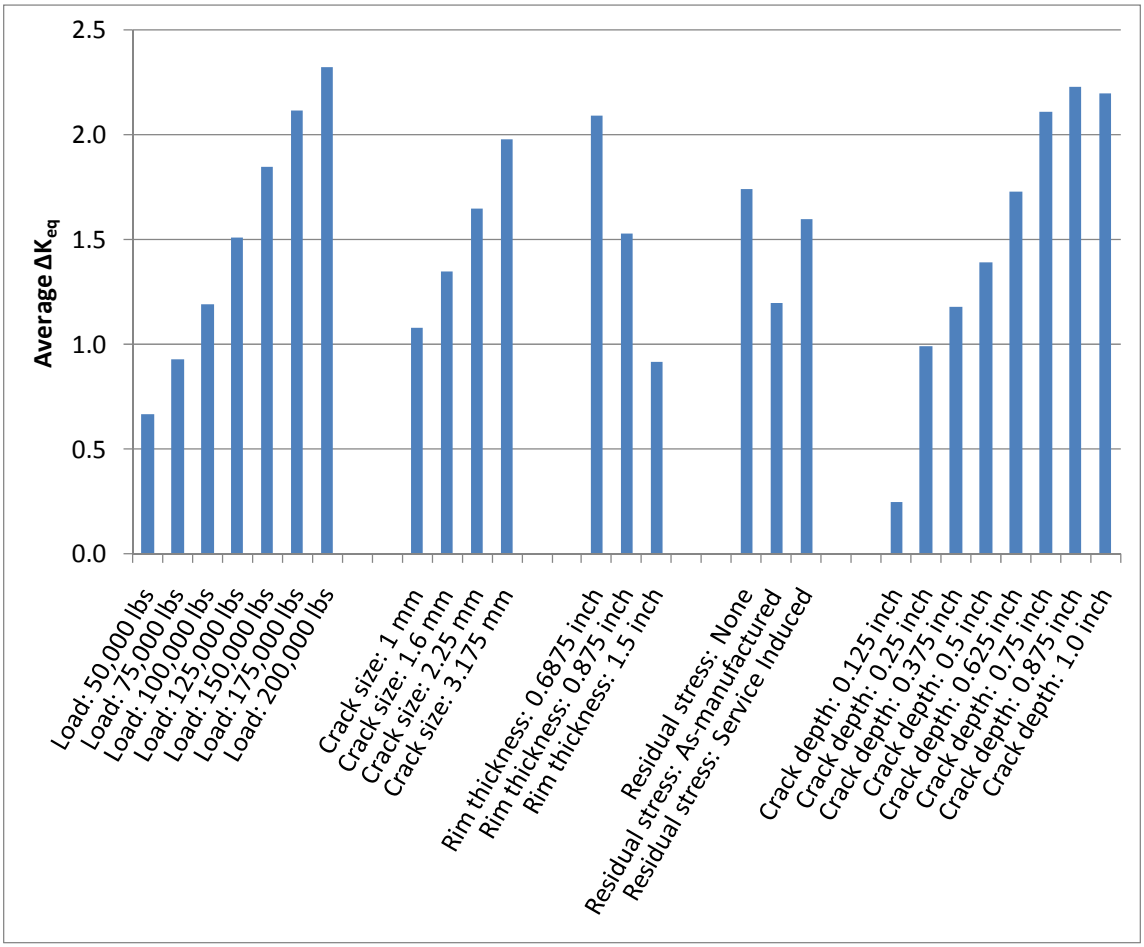

Figure 18 An "effects plot" showing the overall relative effect of each parameter considered.

Fatigue crack growth data of various wheel and rail steels have been reported in the literature [42]. The fatigue crack growth data given in [42] show that the threshold stress intensity factor for various wheel and rail steels ranges between approximately 6 ksi√in and 9 ksi√in depending on the particular steel sample and R-ratio of the test. This threshold stress intensity factor range data was published in 1976 and it would be

beneficial to conduct additional testing considering accurate material composition and for various R-ratios.

Considering a wheel with no residual stress, the equivalent stress intensity factor range (ΔK_{eq}) at the crack tip exceeded 6 ksi√in in the model only when the load was at least 175 kips, the rim was 0.875 in or thinner, and the crack size was 2.25 mm or greater. For wheels with residual stress from manufacturing, the ΔK_{eq} at the crack tip exceeded 6 ksi√in in the model only when the load was 200 kips, the rim thickness was 0.6875 inches, and the crack size was 3.175 mm. Considering wheels with residual stress from manufacturing and service braking, the ΔK_{eq} at the crack tip exceeded 6 ksi√in in the model only when the load was at least 175 kips, the rim thickness was 0.6875 inches, and the crack size was 2.25 mm or greater. The trends from the model suggest that more extreme residual stress states from severe wheel heating in service could potentially yield higher ΔK_{eq} at sub-surface shattered rim crack tips.

4.3.2 Vertical split rim cracking

Wheel loads of 222.41 kN (50 kips) and 444.82 kN (100 kips), and lateral load locations of 25.4 mm (1 in), 38.1 mm (1.5 in), and 44.45 mm (1.75 in) from the front rim face on the tread surface are considered in this section. The crack is always considered at 50.8 mm (2 in) from the front rim face for the sake of illustration. The Hertzian contact parameters for 222.41 kN (50 kips) load are calculated as C_a = 9.4488 mm (0.372 in) and C_b = 7.4676 mm (0.294 in), and for 444.82 kN (100 kips) load as C_a = 11.8872 mm (0.468 in) and C_b = 9.4234 mm (0.371 in), where C_a is the semi-major axis of the

elliptical contact area (along the track direction) and C_b is the semi-minor axis of the elliptical contact area (along the lateral direction).

Figures 19 a-b show the stress results of the full model analysis under a mechanical load of 222.41 kN (50 kips) on the tread surface at 25.4 mm (1 in) from the front rim face without considering any residual stress distribution. The stress contours for rim thickness 38.1 mm (1.5 in), 31.75 mm (1.25 in), and 22.225 mm (0.875 in) are shown in the same order in Figure 18. Figure 19(a) shows the axial stresses in wheel rims. These plots show that higher axial stresses develop in the rim below the load location in a wheel with thinner rim thickness. This high axial stress can develop a high ΔK_I value if a crack, parallel to the front rim face, is present below the load location. Figure 19(b) shows the shear stresses in wheel rims. These plots show that high shear stresses develop close to the load location for all rim thicknesses. This high shear stress can develop a high ΔK_{II} value at the crack tip if a crack is present in this high stress region and can contribute to vertical split rim failure if the ΔK_{II} is higher than the fracture toughness.

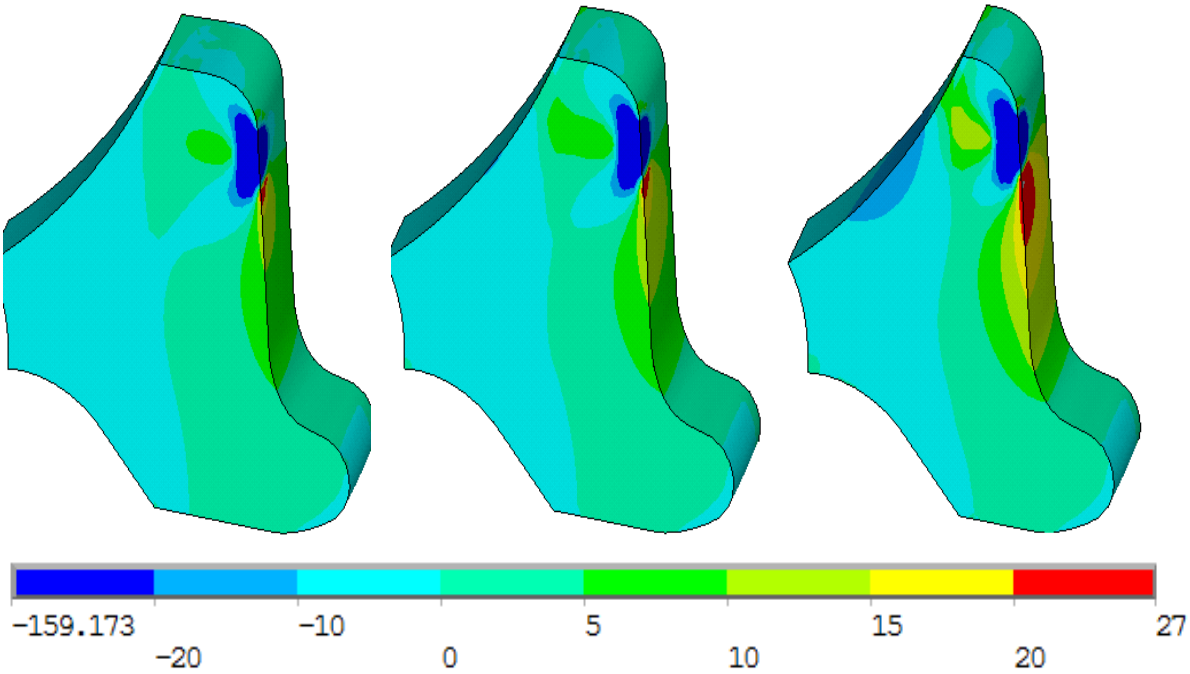

Figure 19(a) Axial stresses (ksi) in the wheel rim under a mechanical load of 222.41 kN (50 kips) at one inch from the front rim face without considering residual stresses.

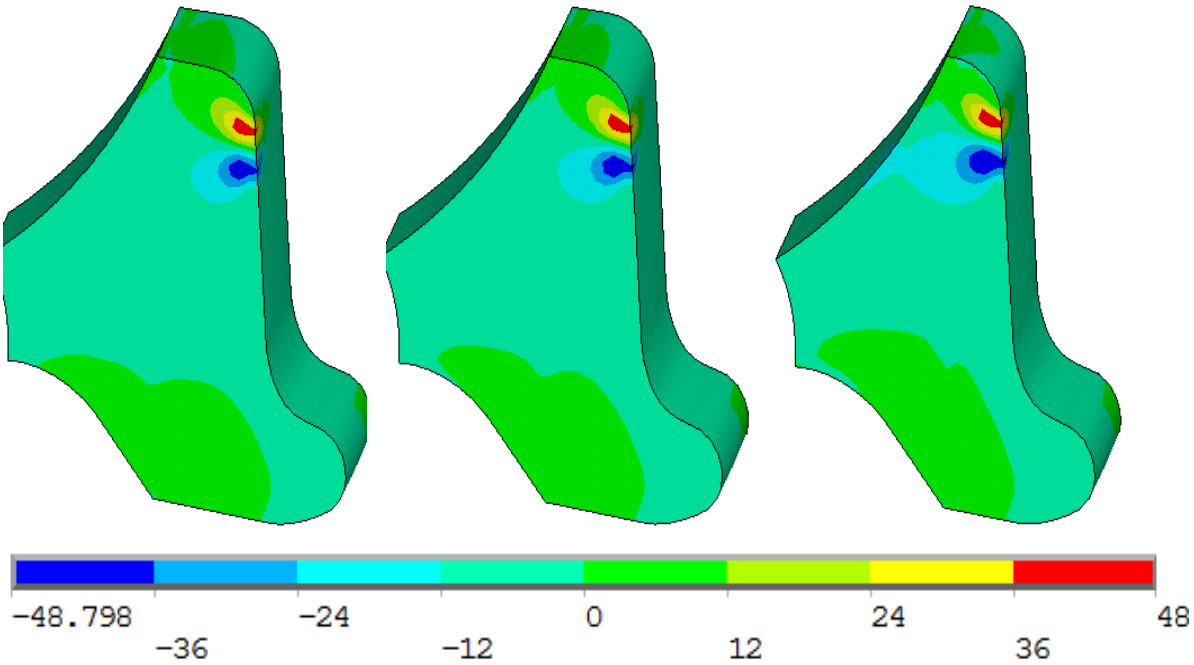

Figure 19(b) Shear stresses (ksi) in the wheel rim under a mechanical load of 222.41 kN (50 kips) at one inch from the front rim face without considering residual stresses.

Figure 20 a-b shows the stress results of the full model analysis under a mechanical load of 222.41 kN (50 kips) on the tread surface at 25.4 mm (1 in) from the front rim face considering as-manufactured residual stress as initial stress to the full model analysis. Figure 20(a) shows the axial stresses in wheel rims. These plots show that the wheel with rim thickness 38.1 mm (1.5 in) has high axial stresses in the rim. The higher the axial stress, the higher the ΔK_I and can contribute to the vertical split rim failure if ΔK_I is greater than the fracture toughness. Although high axial stress is observed in the middle of the rim, vertical split rim cracks have not been observed to start at such depths.

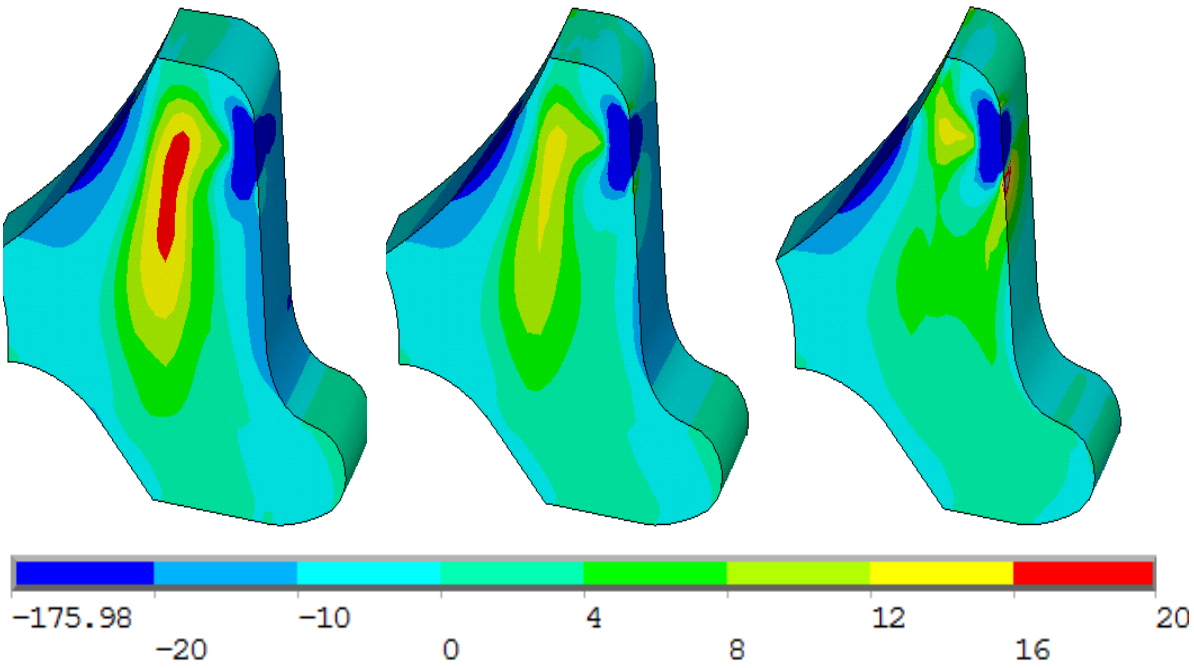

Figure 20(a) Axial stresses (ksi) in the wheel rim under a mechanical load of 222.41 kN (50 kips) at one inch from the front rim face (as-manufactured residual stress as initial stress).

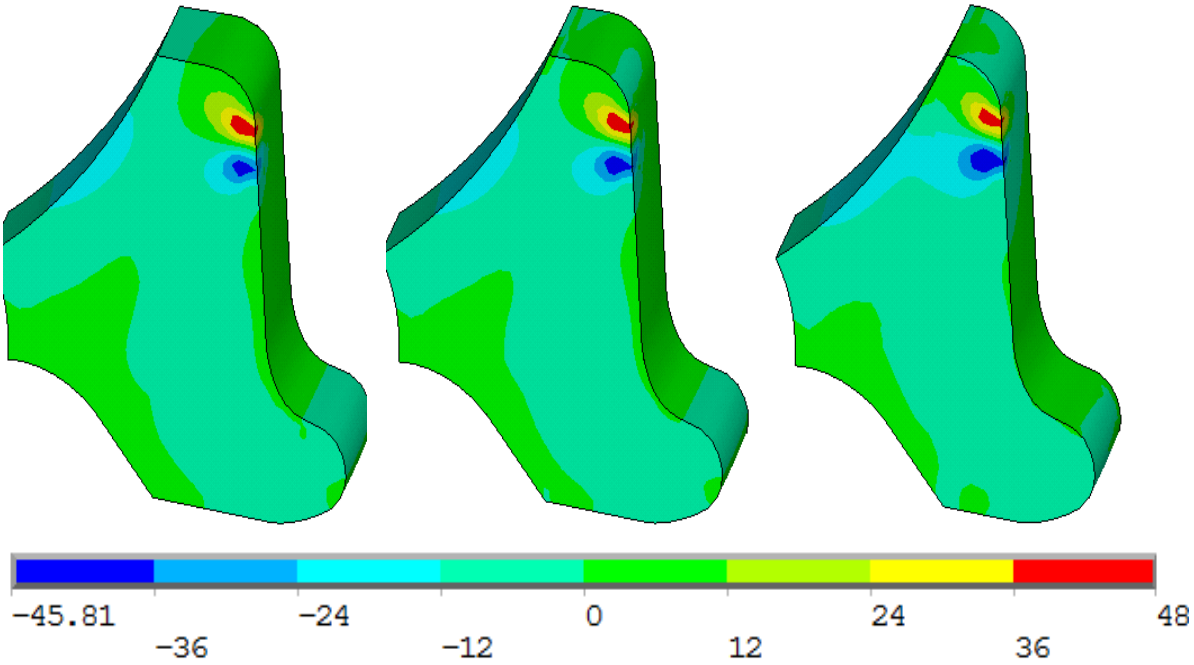

Figure 20(b) Shear stresses (ksi) in the wheel rim under a mechanical load of 222.41 kN (50 kips) at one inch from the front rim face (as-manufactured residual stress as initial stress).

Figures 21 a-b show the stress results of the full model analysis under a mechanical load of 222.41 kN (50 kips) on the tread surface at 25.4 mm (1 in) from the front rim face, including the residual stress developed during both the manufacturing process and the on-tread brake loading for 60 min with a thermal load of 45 HP as the initial stress to the full model analysis.

The full model results are applied as boundary conditions to the sub-model analysis to simulate vertical split rim cracking. The methodology is detailed in Chapter 2. This Chapter considers vertical split rim cracks of sizes 2 mm (0.08 in) and 1 mm (0.04 in) and orientations of 0° and 45° to the front rim face.

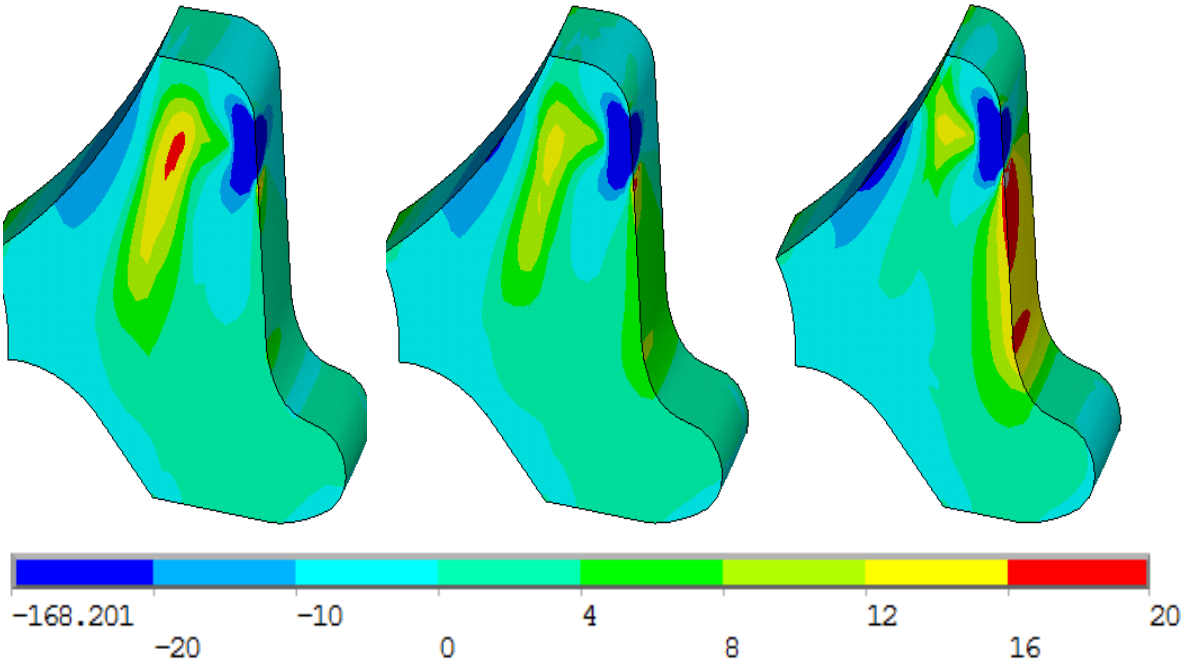

Figure 21(a) Axial stresses (ksi) in the wheel rim under a mechanical load of 222.41 kN (50 kips) at one inch from the front rim face (service-induced residual stress as initial stress).

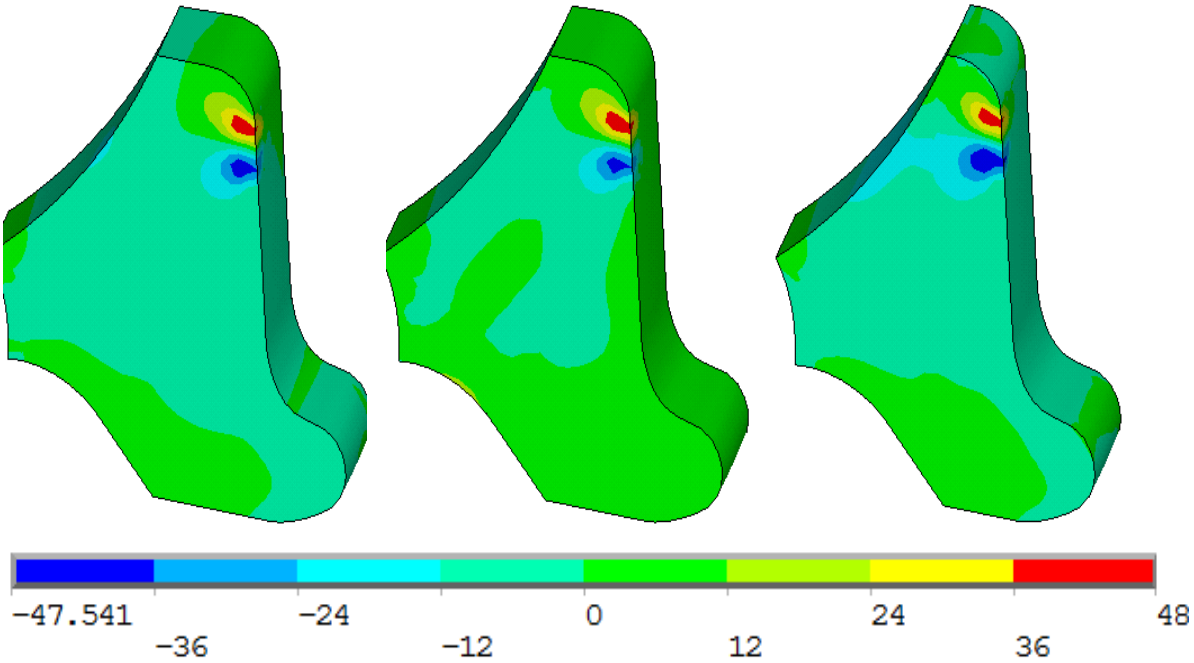

Figure 21(b) Shear stresses (ksi) in the wheel rim under a mechanical load of 222.41 kN (50 kips) at one inch from the front rim face (service-induced residual stress as initial stress).

The fracture toughness of class C wheel steel is 43.8 MPa√m (39.8 ksi√in) [10]. The vertical split rim failure (rapid unstable crack growth) occurs when the equivalent stress intensity factor range at the crack tip exceeds the fracture toughness. Figure 22 shows the ΔK_{eq} variation for a 2 mm (0.08 in) crack parallel to the front rim face under different residual stress states. The crack is located at 50.8 mm (2 in) from the front rim face and oriented at 0° to the front rim face (parallel to the front rim face). The cracks at depths of 3 mm (1/8 in), 6 mm (¼ in), 9 mm (3/8 in), and 12 mm (½ in) from the tread surface are considered. The wheel load of magnitude 222.41 kN (50 kips) is applied at 44.45 mm (1.75 in) from the front rim face.

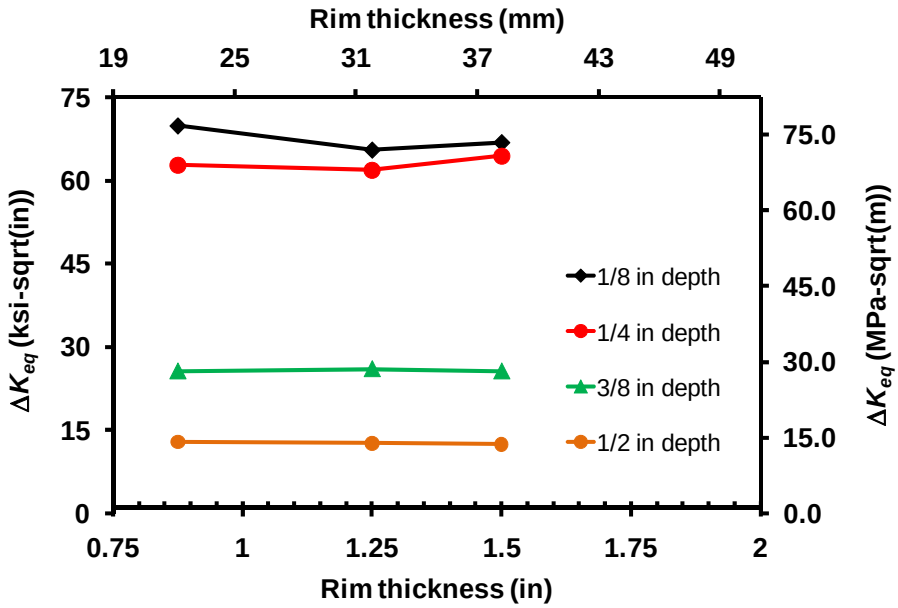

Figure 22(a) Variation of ΔK_{eq} at crack tips with rim thickness (without considering residual stresses).

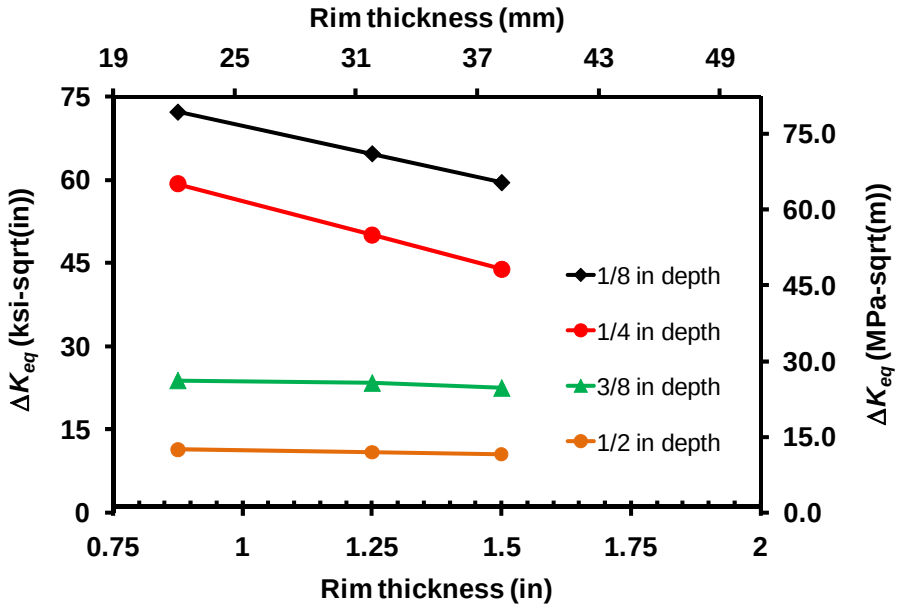

Figure 22(b) Variation of ΔK_{eq} at crack tips with rim thickness (considering as-manufactured residual stress).

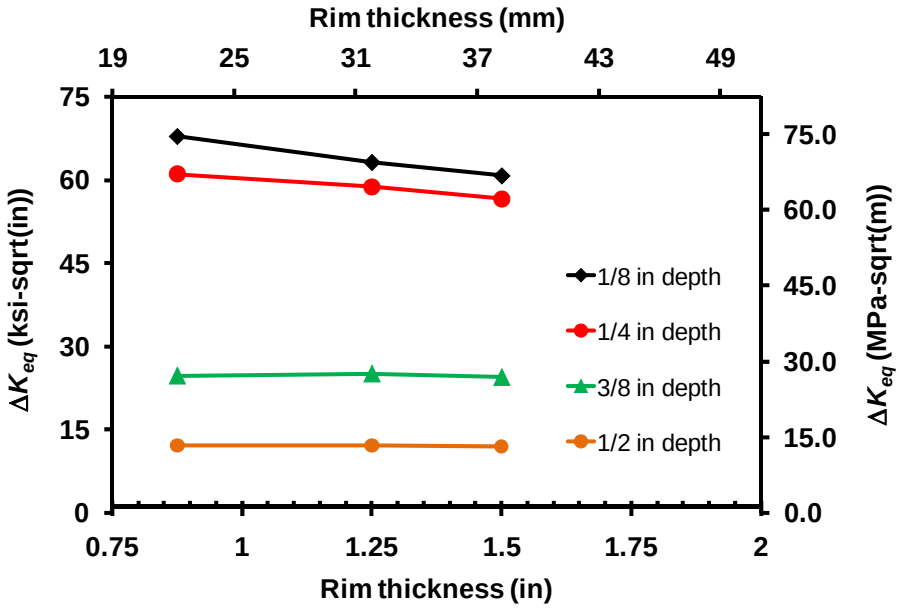

Figure 22(c) Variation of ΔK_{eq} at crack tips with rim thickness (considering both as-manufactured and service-induced residual stress).

This Chapter performed an extensive parametric study, considering different load magnitudes (222.41 kN (50 kips) and 444.82 kN (100 kips)), load locations on the tread

surface (25.4 mm (1 in), 38.1 mm (1.5 in), 44.45 mm (1.75 in) from the front rim face), crack sizes (2 mm (0.08 in) and 1 mm (0.04 in)), crack depths (3 mm (1/8 in), 6 mm (¼ in), 9 mm (3/8 in), and 12 mm (½ in) below the tread surface), and crack orientation (0° and 45° to the front rim face). The crack is always considered at 50.8 mm (2 in) from the front rim face for the sake of illustration. Combination of above variables resulted in a total of 864 simulations. The full model analyses provide the required boundary conditions to the sub-model analyses.

Figure 23 is an "effects plot" showing the overall relative effect of each parameter considered in this analysis. The data in this plot is generated by averaging the stress intensity factor results from all of the analyses in which one variable is held constant. For example, of the 864 total analyses conducted, 432 were conducted with a crack size of 1 mm (0.04 in). Averaging the stress intensity factor results from these 432 analyses gives a result of 12.856 MPa√m (11.7 ksi√in). Likewise, the average stress intensity factor from the 432 analyses with a crack size of 2 mm (0.08 in) gives a result of 18.9 MPa√m (17.2 ksi√in). As mentioned earlier, while this type of plot does not capture all of the interactions occurring between variables, it does give a broad view of the relative importance of each variable on vertical split rim cracking.

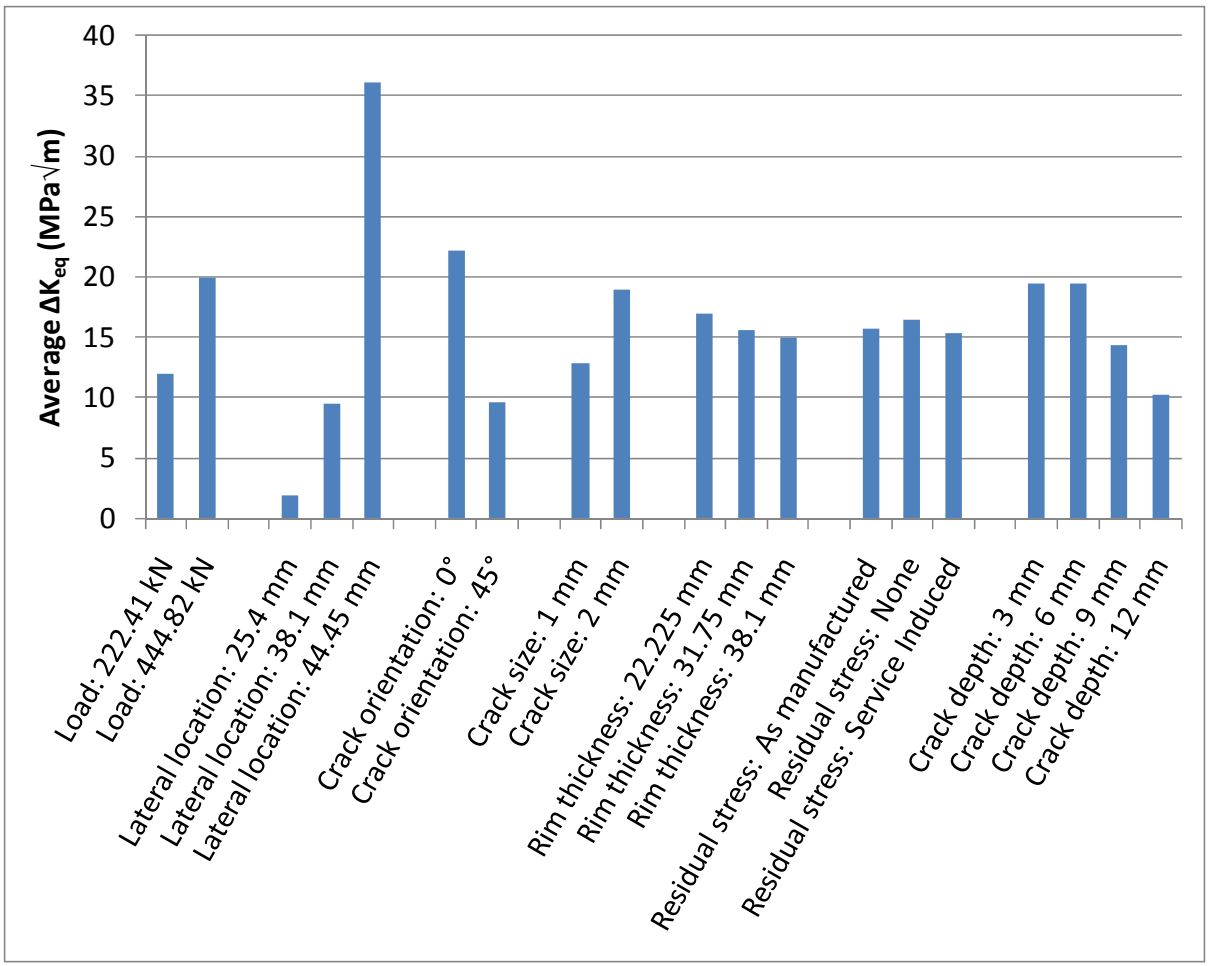

Figure 23 An "effects plot" showing the overall relative effect of each parameter considered.

4.4 Summary and Conclusions

The shattered rim and vertical split rim cracking in railroad wheels are simulated using elastic-plastic finite element analysis and fracture mechanics. The residual stresses developed during both the manufacturing process and under service conditions are considered as initial stresses for the shattered rim cracking analysis. To save computational time, the modeling of shattered rim cracking is divided into two stages: full model and sub-model.

The effect of various parameters, such as wheel rim thickness, residual stresses in the rim (both as-manufactured and service-induced), wheel wear, crack size, and crack vertical location below the tread surface on shattered rim cracking is investigated.

4.4.1 Shattered rim cracking

The effects of various parameters in shattered rim cracking are summarized below:

- *Wheel load* - equivalent stress intensity factor ranges at crack tips increase with increasing wheel load. From Figure 17, it appears that the relationship between wheel load and equivalent stress intensity factor range is approximately linear.
- *Crack size* - ΔK_{eq} at crack tips increase with increase in crack size. The ΔK_{eq} at a crack tip is proportional to the square root of its size. This finding is in good agreement with the theory.
- *Rim thickness* - ΔK_{eq} at crack tips increase significantly with decrease in rim thickness. Figure 17 shows that a non-linear relationship exists between the rim thickness and the ΔK_{eq}. Figure 17 shows rim thickness can be a significant parameter in triggering shattered rim failure.
- *Residual stress state* - Figure 17 shows that the as-manufactured residual stress is beneficial and service-induced residual stresses are detrimental for shattered rim cracking. Consideration of as-manufactured residual stresses decrease the ΔK_{eq} at the crack tip by about 40% compared to that of no residual stress state. Consideration of service-induced residual stresses increase the ΔK_{eq} at the crack tip by about 50% compared to that of as-manufactured residual stress state. This

observation shows that residual stress in the wheel rim is a significant parameter that affects shattered rim failure life.

- *Crack depth* - Figure 17 shows that the sensitive depth for shattered rim cracking ranges from 0.75 in to 0.875 in below the tread surface. This finding is in good agreement with field observations at TTCI.

This above analysis estimated ΔK_{eq} values at subsurface crack tips for different combinations of the above mentioned parameters. Shattered rim crack propagates when ΔK_{eq} at the crack tip exceeds the mode I threshold stress intensity factor range ($\Delta K_{th,I}$) of the wheel material. The conditions (different combination of parameters) that can lead to shattered rim crack propagation can be predicted by comparing the calculated ΔK_{eq} value at the crack tip to the $\Delta K_{th,I}$ of the wheel material.

4.4.2 Vertical split rim cracking

The effects of various parameters on vertical split rim cracking:

- *Relative location of load and crack* - Figure 22 shows that the ΔK_{eq} values for cases with load located at 44.45 mm (1.75 in) from the front rim face are much higher compared to those of cases where load is located at 38.1 mm (1.5 in) and 25.4 mm (1.0 in). The crack is always located at 50.8 mm (2 in) from the front rim face. These results show that the closer the load is to the crack (load located out board from the crack), the higher is probability of vertical split rim cracking. This shows that relative lateral location of load and crack is a critical parameter.

- *Crack orientation* – Figure 22 shows that the ΔK_{eq} values for cases with crack oriented at 0° to the front rim face (parallel to the front rim face) are higher to those of cases where crack is oriented at 45° to the front rim face. These results show that the cracks parallel to the front rim face are critical and can trigger vertical split rim failure; this is consistent with field observations.
- *Load magnitude* – Figure 22 shows that the relationship between the ΔK_{eq} values and the load magnitudes is non-linear, i.e, doubling the load magnitude does not double the ΔK_{eq} values.
- *Crack depth* – Figure 22 shows that the ΔK_{eq} values for cracks at depths 3 mm (0.125 in) and 6 mm (0.25 in) are higher compared to those of cracks at depths 9 mm (0.375 in) and 12 mm (0.5 in). These results show that the cracks at depths up to a 3 mm and oriented 0° to the front rim face (parallel to the front rim face) are critical for vertical split rim cracking. This finding is consistent with the origin of the main fracture of vertical split failures observed in the field.
- *Crack size* – Figure 22 shows that the ratio of the ΔK_{eq} value of crack size 2 mm (0.08 in) to that of a crack size 1 mm (0.04 in) is approximately 1.4 (which is $\sqrt{2}$). This result appears to confirm that the ΔK_{eq} is proportional to $\sqrt{a}$ (square root of crack size). This is in good agreement with the theory.
- *Rim thickness* – Figure 22 shows that the ΔK_{eq} value does not change significantly with the change in rim thickness. This result indicates that rim thickness is not a dominant parameter in triggering vertical split rim failure.

- *Residual stresses* – Figure 22 shows that the variation of ΔK_{eq} with the change in residual stress state is not significant. This result shows that the residual stress state in the rim is not a significant factor in triggering vertical split rim failure.

This above analysis estimated ΔK_{eq} values at subsurface crack tips for different combinations of the above mentioned parameters. Unstable crack growth occurs when ΔK_{eq} at the crack tip exceeds the fracture toughness (K_c) of the wheel material. The conditions (different combination of parameters) that can trigger vertical split rim failure can be predicted by comparing the calculated ΔK_{eq} value at the crack tip to the fracture toughness (K_c) of the wheel material.

CHAPTER 5

PROBABILISTIC FAILURE LIFE PREDICTION

5.1 Introduction

This Chapter predicts railroad wheel failure life considering shattered rim and vertical split rim failures considering realistic service conditions. The failure life depends on several factors, such as the wheel geometry, loading conditions, material defect attributes in the rim, wheel wear, and residual stresses in the rim. Most of these parameters have some randomness under service conditions. This Chapter simulates realistic service conditions by performing probabilistic analysis considering uncertainties in various input parameters.

Shattered rim and vertical split rim cracks are modeled using the methodology detailed in Chapter 2 and the ΔK_{eq} at sub-surface crack tips are estimated. Residual stresses and wheel wear are included in the rolling contact analysis using the methodology detailed in Chapter 3. The ΔK_{eq} values calculated in Chapter 4 are used for failure life prediction.

Under idealistic conditions, railroad wheels experience constant amplitude loading with maximum load being the applied wheel load and minimum being the zero. Sub-surface cracks in the rim experience maximum load when the rail-wheel contact location is close to the sub-surface crack location and minimum (zero load) when the rail-wheel contact location is far away from the sub-surface crack location. However, under realistic service

conditions, railroad wheels experience variable amplitude loading due to occasional over loads and wheel out-of-roundness due to surface defects. This Chapter considers variable amplitude loading to simulate realistic loading conditions. The load histories obtained from wheel impact load detector (WILD) data are used to generate variable amplitude load histories. Variable amplitude loading is applied as block loading on the wheel tread surface. Also, under idealistic conditions, the rail-wheel contact location will be along the taping line. However, under realistic service-conditions, this location can shift laterally due to wheel hunting movement or during a wheel maneuvering over a crossing diamond or over a curve. This lateral shift in rail-wheel contact location can alter contact stresses and stresses near sub-surface crack tips, thereby affecting the wheel failure life. This Chapter considers realistic load locations by considering load location as a random variable.

Under realistic service conditions, sub-surface cracks can be present anywhere in the wheel rim. This condition is simulated by considering crack lateral and vertical locations in the rim as random variables. Also, sub-surface cracks can be oriented in any direction. Based on parametric studies [53,54], sub-surface cracks oriented at an angle of 20° to the tread surface are found to be critical for shattered rim cracking, and those oriented parallel to the front rim face are found to be critical for vertical split rim cracking. These findings are consistent with field observations [21]. Therefore, cracks are assumed to be oriented at critical angles in this Chapter. This conservative assumption reduces the computational effort, by allowing the use of planar crack growth analysis.

This Chapter uses the damage tolerance approach for calculating the wheel failure life. In damage tolerance design, an initial crack is assumed in a component and the failure life is calculated as the number of cycles it takes for the initial crack to reach the critical crack size. In most components, subjected to fatigue loading, crack initiates from a very small material defect (usually smaller than 1 mm (0.04 in) and propagates till the failure. The propagation of cracks smaller than 1 mm is referred to as short crack propagation. The existing linear-elastic fracture mechanics-based crack growth models can only be used for long crack propagation (for crack sizes greater than 1 mm). Ideally, to calculate a component failure life, both short crack propagation and long crack propagation need to be simulated. However, short crack propagation iis complex, anomalous and has high variability. To bypass the short crack propagation region, this Chapter uses an equivalent initial flaw size (EIFS) and considers crack growth model based on linear-elastic fracture mechanics. This approach is detailed in the methodology section.

Under service conditions, the wheel wear depends on several factors, such as the wheel load, track conditions, material properties, applied thermal brake loading, and so forth. The wheel wear volume or wear rate can be calculated using any of the models available in the literature [30]. This Chapter assumes uniform wheel wear for the sake of illustration. The methodology developed in this Chapter to predict the wheel failure life can be used with any of the other wear models available in the literature. However, for cycle-by-cycle failure life calculations, updating the wheel profile using a wear model after each cycle greatly increases the computational time and is practically infeasible.

For a given set of input parameters, such as wheel geometry, loading conditions, sub-surface crack attributes, residual stresses, and wheel wear rate, the ΔK_{eq} at a sub-surface crack tip can be calculated using the methodology detailed in Chapter 2. However, for cycle-by-cycle failure life calculations, the calculation of ΔK_{eq} using finite element analysis and linear-elastic fracture mechanics is computationally expensive. To address this issue, this Chapter replaces the finite element analysis with an inexpensive surrogate model (also referred to as meta model or response surface). There are several types of surrogate models available in the literature, such as polynomial regression, polynomial chaos expansion, Gaussian process interpolation, support vector regression, and relevance vector regression. Sankararaman et al. [43] found the Gaussian process interpolation method to be effective and accurate for ΔK_{eq} calculations. Therefore, a Gaussian process (GP) surrogate model trained using several finite element runs is used to replace the finite element analysis during cycle-by-cycle crack growth analysis.

For a given set of input parameters, a railroad wheel failure life can be calculated using the ΔK_{eq} values calculated using the GP surrogate model and a long crack growth model based on linear-elastic fracture mechanics. There are several crack growth models available in the literature, such as Paris, modified Paris, Waker, NASGRO, Forman, and so forth. NASGRO model can be used for more accurate prediction; however, it is hard to find crack growth model parameters for class C wheel steel. This Chapter considers Walker model for the sake of illustration [21]. The failure life, number of cycles it takes for an initial crack to reach a critical size, is calculated using cycle-by-cycle approach.

In the literature, Liu and Mahadevan [21] have previously performed reliability analysis of railroad wheels considering uncertainties in some of the input variables. However, in that study, residual stresses due to manufacturing and brake loading, and wheel wear were not considered. The wheel loading was assumed to be constant amplitude cyclic loading. A bimodal load distribution was assumed, with the empty car load equal to one-fourth of the full wheel load. The simulation results were able to match the field data only under the unrealistic assumption that 10% of the wheel population has an initial defect size of 10 mm. Also, only shattered rim failure was considered in that study.

This Chapter considers realistic load histories obtained from Wheel Impact Load Detector (WILD) data and also includes wheel wear and residual stresses (both as-manufactured and service-induced) in rolling contact analysis. Both shattered rim and vertical split rim failure modes are considered. Also, assumptions such as 10% of the wheels having an initial defect size of 10 mm and bimodal load distribution are not considered in this Chapter. Thus this Chapter relaxes several limiting assumptions in previous work, and also addresses computational efficiency in the life prediction. The probability distribution for the failure life is obtained by performing Monte Carlo simulations assuming all the input parameters as random variables. For a given sample of input parameters, the smaller of shattered rim failure life and vertical split rim failure life is considered as the wheel failure life. Multiple sets of Monte Carlo simulations are performed to examine the scatter in computed failure lives. The computed results are validated with field data.

5.2 Proposed Methodology

The proposed methodology to predict the failure life consists of four parts: (1) calculation of ΔK_{eq} at the sub-surface crack tip; (2) load history simulation; (3) surrogate model construction; and (4) crack growth life prediction. Each part is discussed below in detail.

5.2.1 Calculation of ΔK_{eq} at the sub-surface crack tip

The methodology to calculate ΔK_{eq} at the sub-surface crack tip (either shattered rim or vertical split rim) was described in detail in Chapter 2.

5.2.2 Load history simulation

Field data obtained from Wheel Impact Load Detectors (WILD) are considered in this Chapter to simulate realistic loading conditions. Figure 24 shows a sample load history [44]. In Figure 24, the x-axis shows dates when the load values are recorded and y-axis shows the corresponding load magnitudes. The loads are recorded once a week. This load history is used to simulate many samples of load histories in this Chapter.

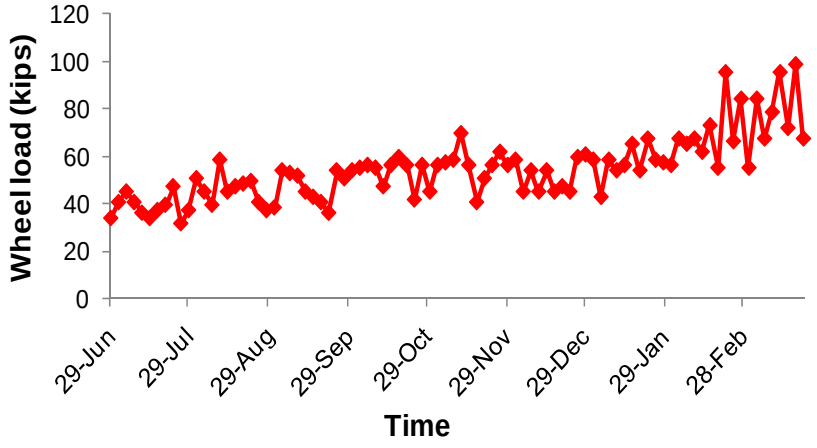

Figure 24. A sample load history obtained from a Wheel Impact Load Detector (WILD) [44]

In the proposed methodology, block loading histories are simulated. The block length is assumed to be a uniform random variable distributed between 100 miles and 2000 miles, which is the distance travelled by a train in a week [45]. A 36 in diameter wheel makes 560 revolutions in a mile. Therefore, number of cycles in a block is uniformly distributed between 56,000 and 1,120,000. The amplitude in each block is assumed to be normally distributed with mean values obtained from the WILD data and 10% coefficient of variation. A small segment of a simulated sample load history is shown in Figure 25. The loading is cyclic since the crack experiences maximum load when the crack is close to the contact surface and experiences zero load when the crack is far from the contact surface due to the wheel rotation.

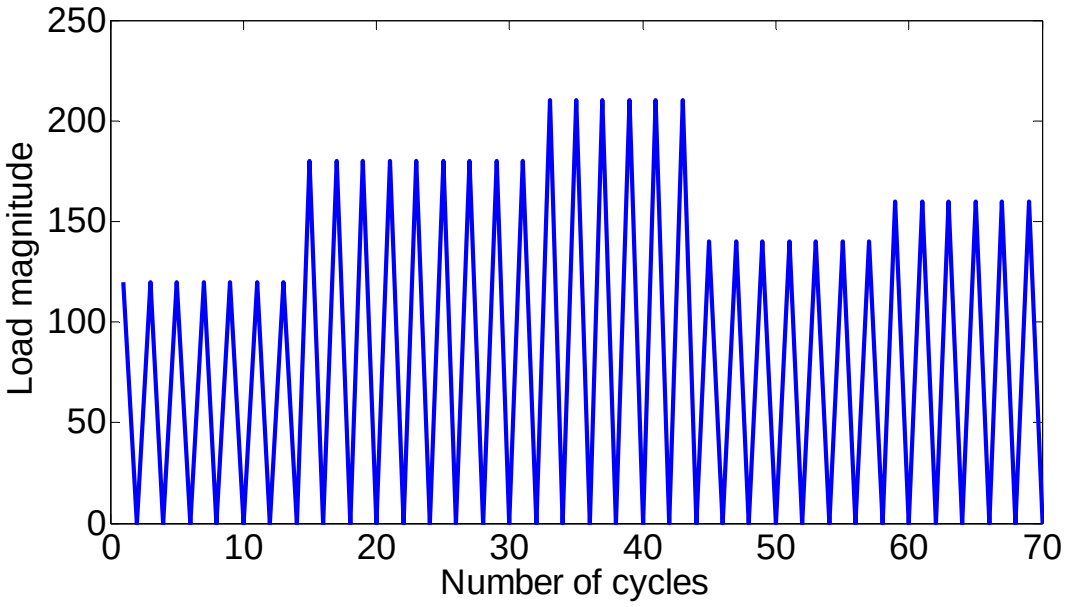

Figure 25. A sample load history showing series of block loads

5.2.3 Surrogate model construction

For a given set of input parameters, ΔK_{eq} can be calculated using the methodology detailed in Chapter 2. For failure life calculations, ΔK_{eq} at the crack tip needs to be calculated after each load cycle, and be used in the crack growth model. Since a repeated evaluation of ΔK_{eq} through cycle-by-cycle finite element analysis is computationally very expensive, it becomes necessary to substitute the expensive finite element analysis with an inexpensive surrogate model (also known as response surface or meta-model).

A Gaussian process response surface approximation is constructed here to capture the relationship between the input variables (wheel rim thickness, load magnitude, load location, crack size, crack location, crack orientation, and residual stress state) and the output variable (ΔK_{eq}), using training points generated by finite element runs at various settings of the input variables.

The basic concept of the GP surrogate model is that the response values Y (ΔK_{eq} in this case), are modeled as a group of multivariate normal random variables, with a defined mean and covariance function. The method is capable of capturing highly nonlinear relationships that exist between input and output variables without assuming an explicit functional form. Additionally, GP models provide a direct estimate of the uncertainty associated with the prediction in terms of variance. The flowchart of GP surrogate model construction is shown in Figure 26. Details of the technique are available in the literature [30, 39-41].

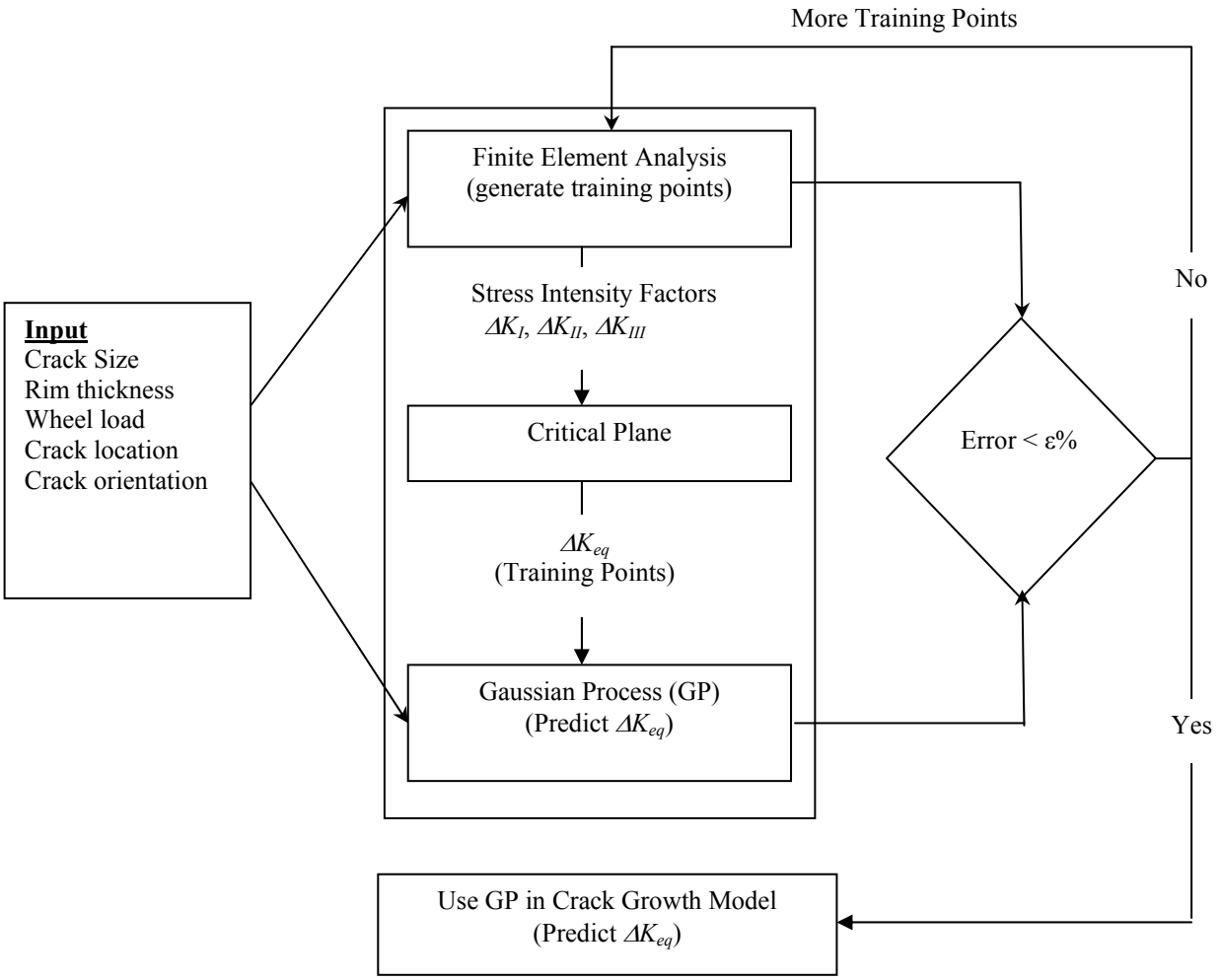

Figure 26. Construction of GP surrogate model for ΔK_{eq} calculations.

Suppose that there are m training points, $x_1, x_2, x_3 \ldots x_m$ of a d-dimensional input variable (the input variables here being the wheel rim thickness, wheel load, crack size, crack location, crack orientation, and residual stress state), yielding the resultant observed random vector $Y(x_1)$, $Y(x_2)$, $Y(x_3)$ … $Y(x_m)$. R is the m x m matrix of correlations among the training points. Under the assumption that the parameters governing both the trend function ($f^T(x_i)$ at each training point) and the covariance (λ) are known, the conditional

expected value of the process at an untested location x^* is calculated as in Eq. (9) and Eq. (10) respectively.

$$Y^* = E\left[Y\left(x^*\right)/Y\right] = f^T\left(x^*\right)\beta + r^T(x^*)R^{-1}(Y - F\beta) \tag{9}$$

$$\sigma^2_{Y^*} = Var\left[Y\left(x^*\right)/Y\right] = \lambda(1 - r^T R^{-1} r) \tag{10}$$

In Eq.(9) and Eq.(10), F is a matrix with rows $f^T(x_i)$, r is the vector of correlations between x^* and each of the training points, β represents the coefficients of the regression trend. McFarland [48] discusses the implementation of this method in detail.

Two separate GP models are constructed here for shattered rim cracking and vertical split rim cracking since the crack orientations that lead to these failures are different. From finite element parametric studies, it is observed that the most critical crack orientation for shattered rim crack growth is 20° to the tread surface, and for vertical split rim crack growth is 90° to the tread surface (0° to the front rim face). This observation is consistent with the field data [52,53,21]. Therefore, this Chapter conservatively assumes these crack orientations to model shattered rim and vertical split rim failure, and uses planar crack growth analysis. A more rigorous alternative is simulation of random crack orientations, and 3-D non-planar crack growth analysis, allowing the cracks to grow into shattered rim and vertical split rim cracks. However, such an approach is computationally very expensive and unaffordable. Figure 27 shows the critical orientations for shattered rim cracks and vertical split rim cracks.

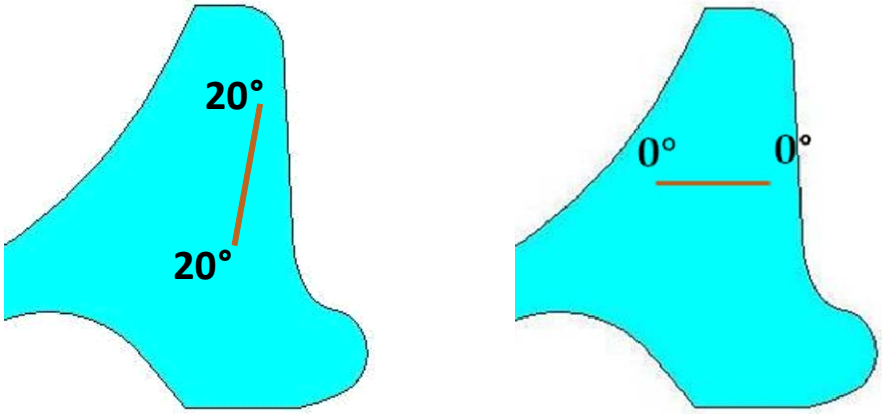

(a) Shattered rim (b) Vertical split rim

Figure 27. Shattered rim and vertical split rim critical crack orientations

5.2.4 Crack growth model and failure life calculation

The rigorous approach to fatigue life prediction would be to perform crack growth analysis starting from the actual initial flaw, accounting for voids and non-metallic inclusions. If the initial crack size is large, then long crack growth models such as Paris's law can be used directly. However, this is not the case in most materials. A schematic plot of the long crack and short crack growth curves is shown in Figure 28.

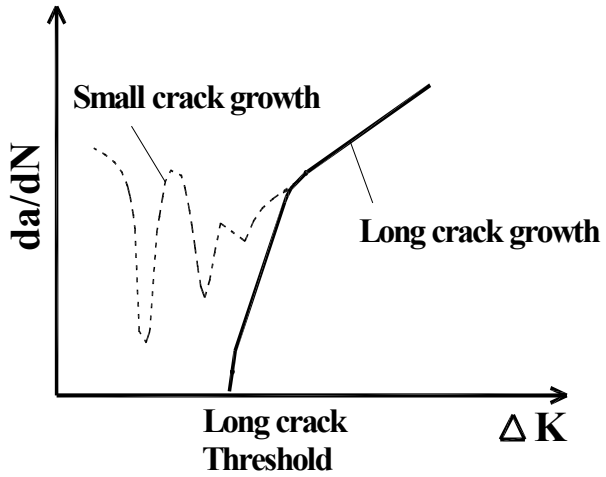

Figure 28. Schematic of Crack Growth

Due to the difficulty in small crack growth modeling, the concept of an equivalent initial flaw size (EIFS) was proposed to bypass small crack growth analysis and make direct use of a long crack growth law for fatigue life prediction. Liu and Mahadevan [21] showed that the equivalent initial flaw size (a_0) can be calculated from material properties (ΔK_{th}, threshold stress intensity factor range and σ_f, fatigue limit) and geometric properties (Y) as

$$a_0 = \frac{1}{\pi}\left(\frac{\Delta K_{th}}{Y\sigma_f}\right)^2 \tag{11}$$

and validated the above formula for several metallic materials [21].

A number of long crack growth models are available in the literature to describe the relationship between da/dN and ΔK, where N represents the number of cycles, a represents the crack size and ΔK represents the stress intensity factor. This Chapter uses Walker's model, only for the sake of illustration [21]. Any other model may also be used instead. Walker's model is expressed as

$$\frac{da}{dN} = C\left(\frac{\Delta K}{(1-R)^{1-P}}\right)^m \tag{12}$$

where C, m, and P are material constants, and R is the stress ratio. The number of cycles (N) to reach a particular crack size a_N can be calculated as

$$N = \int dN = \int_{a_0}^{a_N} \frac{1}{C\left(\frac{\Delta K_{eq}}{(1-R)^{1-P}}\right)^m} da \tag{13}$$

For structures with complicated geometry and loading conditions, the integral in Eq. (13) is to be evaluated cycle by cycle, calculating the stress intensity factor in each cycle of the crack growth analysis. The surrogate modeling described in section 5.2.3 makes this calculation affordable. For shattered rim failure, the failure life is calculated for the crack to reach a size of 1 in. For vertical split rim failure, the failure life is calculated for the crack to reach a critical crack size, when ΔK_{eq} at the crack tip becomes equal to the fracture toughness. Both shattered rim and vertical split rim failure life are estimated for a given set of input parameters, and the smaller of these two is taken as the wheel failure life for the given set of parameter values. Figure 29 shows the various elements of wheel failure life calculation.

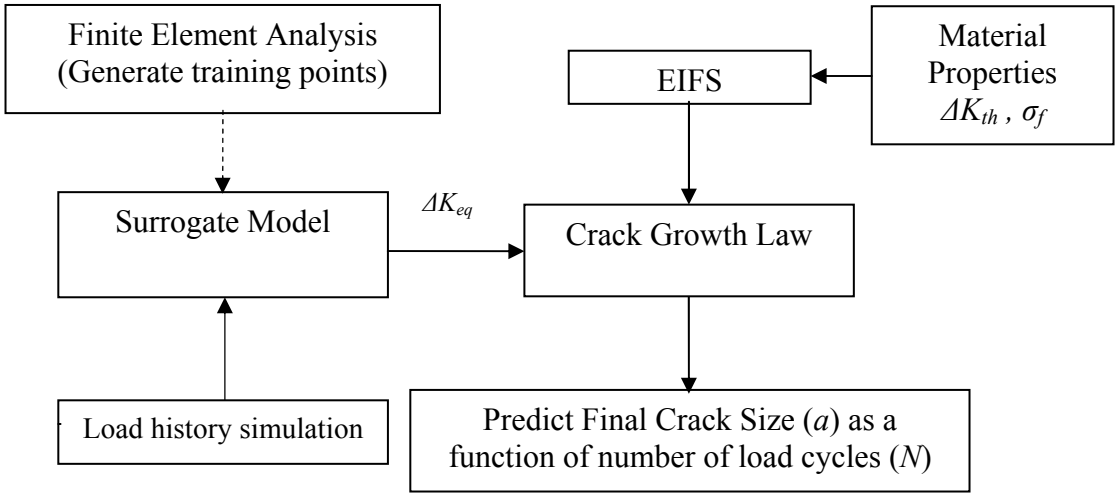

Figure 29 Crack growth life prediction methodology

(Note: Dashed arrow indicates that FEA runs are used only to train the surrogate model. Then life prediction analysis uses only the path through the solid arrows).

5.3 Numerical Implementation

5.3.1 Investigation of significant factors

Chapter 4 performed extensive parametric studies to understand the effect of various input parameters on shattered rim and vertical split rim cracking. Some more numerical simulations are performed in this chapter to train and verify the GP surrogate model. The parameters considered for these additional simulations are described in the next sub-section.

5.3.2 Surrogate model construction

Gaussian process surrogate models are constructed and verified using the data obtained from finite element analyses. The inputs for the Gaussian process models are rim thickness (wheel wear can be considered by reducing the rim thickness), load magnitude, load lateral location, crack lateral location, crack vertical location, and crack size. The crack orientation is assumed to be either 20° to the tread surface (for shattered rim crack) or parallel to the front rim face (for vertical split rim crack). The data obtained from finite element analysis considering both as-manufactured and service-induced residual stresses are used for constructing Gaussian process models. A constant wheel wear rate of 3 μm per 10^5 cycles is assumed. Gaussian process models for both shattered rim and vertical split rim are trained with 1944 training points and verified with an additional set of 288 points. Tables 10 and 11 list the various parameter values considered for GP model training and verification. The training data and verification data are independent of each other, different combination of given input parameters leads to different combination.

Table 10 Input parameter values considered for shattered rim GP model

Input parameter	Training values	Verification values
Rim thickness (in)	0.6875, 0.875, 1.5	0.875, 1.25, 1.5
Load magnitude (kips)	32.5, 75, 100	50, 75
Lateral load location (in)	1, 1.75, 2	1.5, 1.75
Lateral crack location (in)	1, 1.75, 2	1.5, 1.75
Vertical crack location (in)	0.125, 0.5, 0.75, 1	0.25, 0.375, 0.625, 0.875
Crack sizes (mm)	0.1, 1, 2.25, 5, 15, 25	1.6, 3.2, 10

Table 11 Input parameter values considered for vertical split rim GP model

Input parameter	Training values	Verification values
Rim thickness (in)	0.875, 1.25, 1.5	0.875, 1.25, 1.5
Load magnitude (kips)	32.5, 75, 100	50, 75
Lateral load location (in)	1, 1.75, 2	1.5, 1.75
Lateral crack location (in)	1, 1.75, 2	1.5, 1.75
Vertical crack location (in)	0.125, 0.25, 0.5, 1	0.375, 0.625, 0.75, 0.875
Crack sizes (mm)	0.1, 1, 2.25, 5, 15, 25	1.6, 3.2, 10

Figures 30 a-b show the plots of ΔK_{eq} values obtained from finite element analysis vs. GP model for shattered rim and vertical split rim cracking respectively. These plots show that GP model prediction is in reasonably good agreement with the finite element values. The error for the shattered rim GP model is within 15% and the coefficient of variation ranges from 0.06 to 0.17. The error for the vertical split rim GP model is within 10% and the coefficient of variation ranges from 0.07 to 0.13. With these statistics, these GP models are assumed to be adequate and used in further analysis. Additional data could be collected to train the surrogate model for higher accuracy and precision if desired.

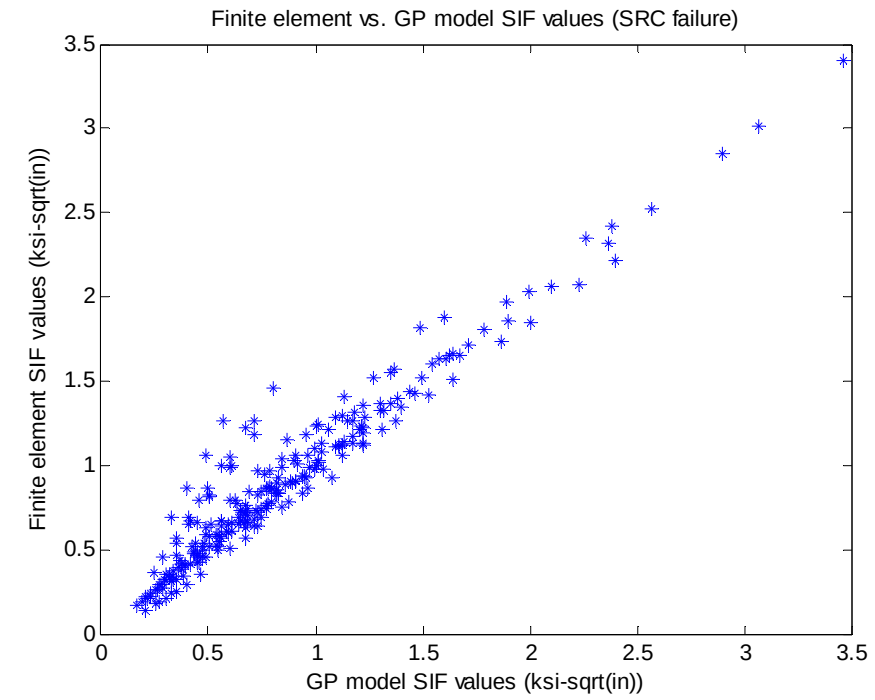

Figure 30(a) Plot of ΔK_{eq} (ksi$\sqrt{}$in) values calculated using finite element model vs. ΔK_{eq} (ksi$\sqrt{}$in) values calculated using GP model built for SRC failure.

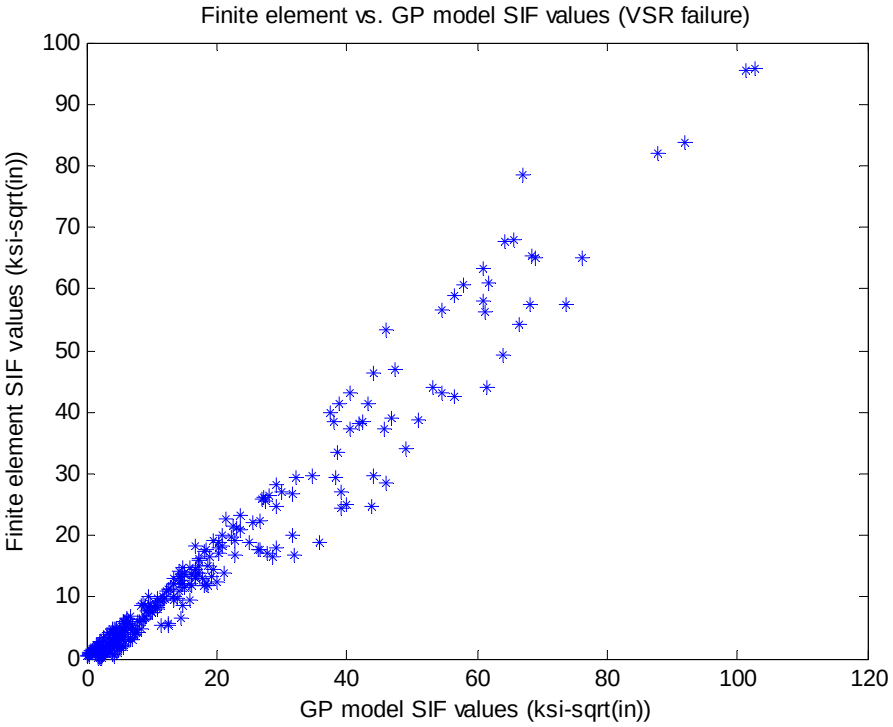

Figure 30(b) Plot of ΔK_{eq} (ksi$\sqrt{}$in) values calculated using finite element model vs. ΔK_{eq} (ksi$\sqrt{}$in) values calculated using GP model built for VSR failure.

5.3.3 Failure life prediction

Wheel failure life is estimated using ΔK_{eq} values calculated from the Gaussian process surrogate model and Walker's crack growth model by performing cycle-by-cycle crack growth calculations. The failure life is the number of cycles it takes for an initial crack size to reach the critical crack size. The smaller of shattered rim and vertical split rim failure lives is considered as the failure life for a given sample of input parameter values. Monte Carlo simulations are performed to estimate the probability distribution of the failure life considering uncertainties in the input parameters. Multiple sets of Monte Carlo simulations are performed to examine the scatter in the computed failure lives.

The EIFS is assumed to be distributed lognormally with a mean value calculated using Eq. (11) and a coefficient of variation of 0.1. The crack growth model parameters C, m, and p are assumed to be normally distributed with 10% coefficient of variation. Sub-surface cracks are assumed to be uniformly distributed in both lateral (between taping line and 1 in from the front rim face) and vertical directions (between 1/8 in to 1 in from the tread surface). The lateral load location on the tread surface is assumed to be uniformly distributed. The crack orientation is assumed to be either critical shattered rim crack orientation (20° to the tread surface) or critical vertical split rim crack orientation (90° to the tread surface). Figure 31 (a) shows the histogram of computed failure lives.

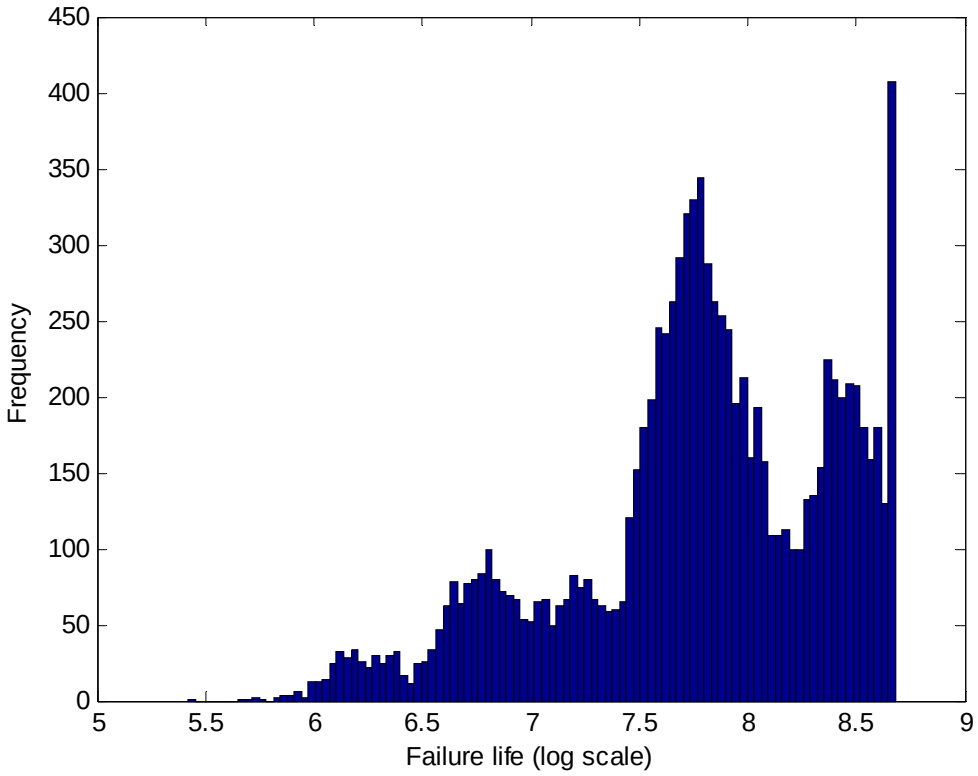

Figure 30(a) Histogram for one Monte Carlo simulation of predicted failure life values

In the literature [50], it was reported that a typical railroad wheel failure life ranges between 250,000 miles and 500,000 miles ($10^{8.146}$ – $10^{8.45}$) depending on the operating conditions. The results in Figure 17(a) are reasonably in good agreement with the observation in [50]. The computed results are conservative since the analysis considered only load histories with high load magnitude obtained from WILD. These high loads are experienced by the wheel only when there is wheel out-of-roundness due to surface defects or shelling/spalling. The observation in [50] is based on general wheel population. The computed results are also conservative due to additional assumptions, which are discussed below. Also, Figure 30(a) shows that about 4.25% (the last bar in the histogram) of the predicted failure lives are due to wheel wear.

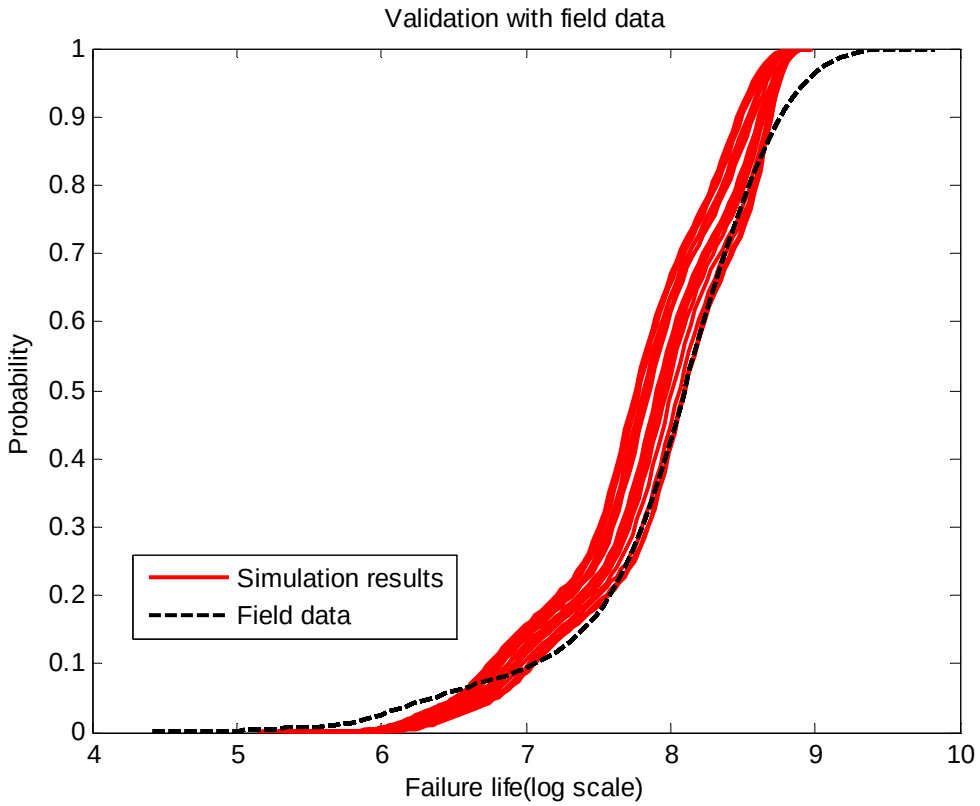

Figure 30(b) Comparison of simulation results with field data

Figure 30(b) compares the computed lives with field data and also shows the scatter in the computed results (20 realizations with 10,000 Monte Carlo simulations each). Field data consisting of 150 failed wheel lives is used to compare against the simulation results [21]. This field data comprises of wheel lives that are failed due to all possible wheel failure types, and classification of field data into specific failure types is not available. The scatter in the computed mean, 5%, and 95% failure lives are about 4%, 4.5%, and 1.5% respectively. The simulation results are close to field data but on the conservative side. The conservatism is due to some of the assumptions made in the analysis. The analysis considered cracks with critical orientations only. Sub-surface cracks oriented at

an angle of 20° to the tread surface are critical for shattered rim cracking and oriented parallel to the front rim face are critical for vertical split rim cracking. For a given set of input parameters, the crack is assumed to be oriented at one of these critical orientations and planar crack growth analysis is used. Since sub-surface cracks can be oriented in any direction, this assumption makes the simulation results conservative compared to field data. Also, the analysis assumes the worst possible thermal brake loading (thermal load of 45 HP for duration of 60 min) on a wheel, which is a conservative assumption. In addition uniform wheel wear is assumed, which is also conservative. However, even with the above mentioned conservative assumptions and analysis simplifications, the analysis results are remarkably close to field data

5.4 Summary and Conclusions

This Chapter developed probabilistic methodology for the prediction of railroad wheel failure life under realistic service conditions. Shattered rim and vertical split rim cracking, two dominant failure types, are modeled using three-dimensional finite element analysis and a mixed-mode crack model based on critical plane concepts. Residual stresses (both as-manufactured and service induced) are included as initial stresses for rolling contact analysis. Several realistic conditions, such as variable amplitude loading, consideration of wheel wear, and variations in sub-surface crack locations and load transfer locations are considered. Failure life distribution is obtained by performing Monte Carlo simulations using an inexpensive surrogate model trained using finite element results. The scatter in the computed failure lives is examined by performing multiple sets of Monte Carlo simulations.

Several input parameters and crack growth model parameters are assumed to have a coefficient of variation of 10% for the sake of illustrating the proposed methodology. Variable amplitude loading is modeled as block loading and the number of cycles in a block is assumed to be uniformly distributed. Graphical comparison between the simulation results and field data shows that the proposed failure life prediction methodology captures the field-observed failure behavior very well. The simulation results are a little conservative compared to field data, and are attributable to several assumptions.

One simplifying conservative assumption is that the shattered rim and vertical split rim cracks are assumed to be oriented at their respective critical orientations and the resulting use of planar crack growth analysis. A more rigorous alternative is simulation of random crack orientations, and 3-D non-planar crack growth analysis, allowing the cracks to grow into shattered rim and vertical split rim cracks. Another assumption is the consideration of worst possible thermal brake loading (thermal brake load of 45 HP for 60 min), which is conservative. A more rigorous alternative is to apply thermal brake loading as a variable amplitude thermal loading based on field data. A third conservative assumption is uniform wheel wear. A more rigorous alternative is to update the wheel profile after each cycle using a wear model. A fourth conservative assumption is consideration of load histories with relatively very high load magnitudes. These high load values are observed only when there is wheel out-of-roundness due to surface defects or shelling/spalling. A more rigorous alternative is to consider all possible load histories

obtained from WILD. However, these alternatives are computationally very expensive, whereas the method developed in this Chapter appears to have good agreement with field data. Thus the proposed method provides a reasonable balance between realistic modeling and computational effort.

CHAPTER 6

SUMMARY AND CONCLUSIONS

This dissertation has developed a general methodology to predict railroad wheel failure life using the damage tolerance approach. This research considered shattered rim failure and vertical split rim failure, the two most dominant failure types observed in North America. Shattered rim and vertical split rim failures occur due to the propagation of sub-surface crack.

The sub-surface cracking is modeled using three-dimensional, multi-resolution finite element analysis and a mixed-mode crack model based on critical plane concepts. For computational efficiency, the finite element analysis is divided in to two stages: full model analysis and sub-model analysis. In the full model analysis, complete wheel geometry is considered and rolling contact analysis is performed. The wheel load on the tread surface is applied using Hertzian contact theory. In the sub-model analysis, a small block with an embedded 3D fatigue crack is considered and elastic-plastic analysis is performed to estimate the uni-modal stress intensity factor ranges at the crack tip. The results from the full model are applied as boundary conditions to the sub-model. A mixed-mode crack model based on critical plane concepts is used to compute the equivalent stress intensity factor range (ΔK_{eq}) at the crack tip using the uni-modal values obtained from the finite element analysis. The methodology developed in Chapter 2, to

calculate ΔK_{eq} at sub-surface crack tips (shattered rim and vertical split rim) is useful in predicting the shattered rim and vertical split rim failure life.

Residual stresses in the wheel rim can affect the ΔK_{eq} at a sub-surface crack tip, and thereby the wheel failure life. Therefore, residual stresses developed during both the manufacturing process and due to the thermal brake loading under service conditions, are estimated using three-dimensional decoupled thermal-structural finite element analyses, and these estimated results are included as initial stresses for rolling contact analysis. Transient thermal analysis of the manufacturing process is performed considering different convection boundary conditions. Non-linear elastic-plastic structural analysis of the manufacturing process is performed by applying the estimated temperatures as body loads. The resultant stress is the as-manufactured residual stress. Transient thermal analysis of the thermal brake loading is performed considering different convection and heat flux boundary conditions. Non-linear elastic-plastic structural analysis of the thermal brake loading is performed by applying the estimated temperatures as body loads and including the estimated as-manufactured residual stress as initial stress. The resultant stress is the residual stress developed due to both the manufacturing process and the thermal brake loading under service conditions. Creep effects are considered in estimating both as-manufactured residual stress and service-induced residual stress using Gallagher's creep model.

This research assumed uniform wheel wear for the sake of illustration. However, the methodology developed is applicable considering any other wheel wear models available

in the literature. Residual stresses are dependent on the rim thickness as the wheel wear removes the outer strip of the stresses and forces residual stress re-distribution in the wheel rim. Residual stresses in a thinner rim wheel are estimated using decoupled thermal-structural analyses and sub-modeling techniques. The estimated residual stresses are applied as initial stresses for rolling contact analysis.

Chapter 4 investigated the effect of various parameters on sub-surface cracking (shattered rim and vertical split rim cracking). The sub-surface crack propagation rate depends on several parameters, such as wheel geometry (diameter, rim thickness, and plate design), loading conditions (magnitude and location), residual stresses in the rim (as-manufactured and service conditions), wheel wear, and sub-surface crack attributes (size, shape, location, and orientation). Numerical studies are performed to estimate the ΔK_{eq} values at various sub-surface cracks considering different possible combination of input parameters. The results show that rim thickness and residual stresses are the two most significant parameters that can affect shattered rim cracking. The significant parameter for vertical split rim cracking is the relative location between the applied load and sub-surface crack location. The results show that rim thickness and residual stresses might not be significant parameters for vertical split rim cracking.

Chapter 5 developed a general methodology to predict the failure life of railroad wheels considering uncertainties in the loading and other possible sources. Shattered rim and vertical split rim cracks were modeled using the methodology detailed in Chapter 2. Residual stresses estimated in Chapter 3 were included as initial stresses for the cracking

analysis. The ΔK_{eq} values at sub-surface crack tips under different input conditions calculated in Chapter 4 were used in predicting the failure of railroad wheels. This chapter predicted the failure life under realistic conditions, such as variable amplitude wheel loading, inclusion of residual stresses (as-manufactured and service-induced) as initial stresses, consideration of wheel wear, sub-surface cracks randomly distributed in the rim, and so forth. Since finite element analysis to estimate ΔK_{eq} at a sub-surface crack for cycle-by-cycle calculations is computationally expensive, a Gaussian process surrogate model was developed to represent the relationship between the above mentioned input parameters and ΔK_{eq} at the crack tip. Load histories obtained from wheel impact load detector (WILD) data were used to generate variable amplitude load histories for rolling contact analysis. The uncertainties in various input parameters are considered through probabilistic analysis. For a given set of input parameters, the minimum of shattered rim and vertical split rim failure life is considered as the wheel failure life. Monte Carlo simulations are performed to obtain the failure life probability distribution. The numerical results are validated using field data.

This dissertation has not considered less dominant failure types, such as shelling and spalling. Further study is required to address these types of failures. Deterministic residual stresses are considered in Chapter 3. However, there is variability in both as-manufactured and service-induced residual stresses. Variability in manufacturing conditions, such as quenching duration, tempering duration, ambient temperatures, draw furnace temperature, and other factors can induce variability in as-manufactured residual stresses. Variability under service conditions, such as braking duration, applied load, and

other factor can induce variability in service-induced residual stresses. Further study is required to address variability in residual stresses. This research has considered only loads in the vertical direction (perpendicular to the rail) and has not considered any lateral load on the wheel flange. Wheel flange can experience lateral loading due to wheel hunting movement. Further study is required to address this issue. In addition to natural variability, probabilistic life prediction is also affected by data uncertainty (due to sparse data) and model uncertainty (assumptions and approximations). Future work may investigate efficient methods to incorporate more realistic modeling, and develop data to support random variable treatments of the variables affecting the failure life.

REFERENCES

[1] Tournay, H, M., Mulder, J, M., "The transition from the wear to the stress regime," Wear, Vol. 191, pp. 107-112, 1996.

[2] Johnson, K, L., "The strength of surfaces in rolling contact, Proceedings of the Institute of Mechanical Engineering," IMechE, pp. 203:151-63, 1989.

[3] Ekberg, A., Kabo, E., "Fatigue of railway wheels and rails under rolling contact and thermal loading – an overview," Wear, Vol. 258, Issue 7-8, pp. 1288-300, 2005.

[4] Liu, Y., Stratman, B., Mahadevan, S., "Fatigue crack initiation life prediction of railroad wheels," International Journal of Fatigue, Vol. 28, Issue 7, pp. 747-756, 2006.

[5] Stone, D, H., Majumder, G., Bowaj, V, S., "Shattered rim wheel defects and the effect of lateral loads and brake heating on their growth," ASME International Mechanical Engineering Congress & Exposition. New Orleans, Louisiana, 1-4, November, 2002.

[6] Giammarise, A, W., Gilmore, R, S., "Wheel Quality: A North American Locomotive Builder's Perspective," GE Research & Development Center, CRD 140, Sep, 2001.

[7] Stone, D., Lonsdale, C., Kalay, S., "Effect of wheel impact loading on shattered rims," Proceedings of 13th International Wheelset Congress, Rome, 2001.

[8] Stone, D, H., and Dahlman, G, E., "The effect of discontinuity size on the initiation of shattered rim defects," ASME Rail Transportation Division, Vol. 19, pp. 7-14, 2000.

[9] Beretta, S., Donzella, G., Roberti, R., and Ghidini, A., "Deep shelling in railway wheels," Proceedings of the 13th International Wheelset Congress, Italy, Chapter 23, 2001.

[10] Kabo, E., and Ekberg, A. "Material defects in rolling contact fatigue of railway wheels – the influence of defect size," Wear, Vol. 258, Issues 7-8, pp. 1194-1200, 2005.

[11] Lunden, R., "Cracks in railway wheels under rolling contact load," Proceedings of the 10th International Wheelset Congress, Australia, pp. 163-8, 1992.

[12] Marais, J, J., "Wheel failures on heavy haul freight wheels due to subsurface defects," Proceedings of the 12th International Wheelset Congress, China, pp. 306-14, 1998.

[13] H. Tournay, Report on Shattered Rim Cracks Observed at TTCI, Personal Communication, TTCI, Pueblo, Colorado, 2007.

[14] C.P. Lonsdale, T. Rusin, T. Hay, Research to Understand the Effects of Wheel Impact Loads on Wheel Stress Levels, Proceedings of the ASME Joint Rail Conference, Pueblo, Colorado, March 3-5, 2009.

[15] D. Stone, S. Dedmon, J. Pilch, S. Cummings, Vertical Split Rim Wheels, Proceedings of the 16th International Wheel Set Congress, Cape Town, March 14-19, 2010.

[16] Derailment Report. Report Number: R94W0019, Rail, January 23, 1994.

[17] Derailment Report. Report Number: R00Q0023, Rail, May 22, 2000.

[18] Theory Reference, Release 11.0, ANSYS, Inc., 2009.

[19] Johnson, K. L., "Contact Mechanics," pp.452, 1987.

[20] Liu, Y., and Mahadevan, S., "Threshold intensity factor and crack growth rate prediction under mixed-mode loading," Engineering Fracture Mechanics, Vol. 74, pp. 332-345, 2007.

[21] Liu, Y., and Mahadevan, S., Multiaxial high-cycle fatigue criterion and life prediction for metals. International Journal of Fatigue, Vol. 7, Issue 7, pp. 790-800, 2005.

[22] ElHaddad, M. H., Topper, T. H., and Smith, K. N., "Prediction of non-propagating cracks," Engineering Fracture Mechanics, Vol. 11, pp. 573-584, 1979.

[23] Kitagawa, H., and Takahashi, S., Applicability of fracture mechanics to very small cracks or cracks in early stage. In: Proceedings of 2nd International conference on mechanical behavior of materials, Metal Park (OH, USA): ASM International, pp. 627-631, 1976.

[24] Tada, H., Paris, P. C., and Irwin, G. R., "The Stress Analysis of Cracks Handbook," pp. 342,363 Third Edition, 2000.

[25] Wang, K., "The Probabilistic Study of Heat Treatment Process for Railroad Wheels Using ANSYS/PDS," Proceedings of the 13th International ANSYS Conference, Pittsburgh, PA, May, 2006.

[26] Lonsdale, C. P., Demilly, F., and Fabbro, V. D., "Wheel Rim Residual Stress Measurements," Proceedings of the Railway Wheel Manufacturer's Engineering

Committee Technical Conference, C. P. Lonsdale., eds., Chicago, Illinois, September 19, 2000.

[27] Gordon, J., and Perlman, A. B., "Estimation of Residual Stresses in Railroad Commuter Car Wheels Following Manufacture," Proceedings of the International Mechanical Engineering Congress and Exhibition, ASME Rail Transportation Division Conference, E. J. Wolf., eds., Vol. 15, pp. 13-18, Anaheim, CA, November, 1998.

[28] Gordon, J., Jones, J. A., and Perlman, A. B., "Evaluation of Service-Induced Residual Stresses in Railroad Car Commuter Wheels," Proceedings of the International Mechanical Engineering Congress and Exhibition, ASME Rail Transportation Division Conference, E. J. Wolf., eds., Vol. 15, pp. 25-32, Anaheim, CA, November, 1998.

[29] Gordon, J., 1998, "Estimation of Residual Stresses in Railroad Car Wheels Resulting from Manufacture and Service Loading," M.S. thesis, Tufts University, Medford, MA.

[30] Tunna, J., Sinclair, J., and Perez, J., "A Review of Wheel Wear and Rolling Contact Fatigue," Proceedings of the Institution of Mechanical Engineers, Part F: Journal of Rail and Rapid Transit, Vol. 221, pp. 271-89, February, 2007.

[31] Dedmon, S. L., Pilch, J., and Gordon, J., "Development of Residual Stresses in a Railroad Wheel through Rim Spray Heat Treatment," Proceedings of the ASME Rail Transportation Division (RTD) Conference, Chicago, IL, September 24-25, 2008.

[32] Wang, K., and Pilon, R., "Investigation of Heat Treating of Railroad Wheels and Its Effect on Braking Using Finite Element Analysis," Proceedings of the International ANSYS Conference, Pittsburgh, PA, April, 2002.

[33] Liu, S., Perlman, B., and Gordon, J., "Residual Stresses in Passenger car Wheels," Proceedings of the International Mechanical Engineering Congress and Exhibition, Chicago, IL, November 5-10, 2006.

[34] Kuhlman, C., Sehitoglu, H., and Gallagher, M., "The Significance of Material Properties on Stresses Developed During Quenching of Railroad Wheels," Proceedings of the ASME Railroad Conference, pp. 55-63, April, 1988.

[35] Association of American Railroads, Manual of Standards and Recommended Practices: Section G- Wheels and Axles, 1998.

[36] Enblom, R., and Berg, M., "Emerging engineering models for wheel/rail wear simulation," Proceedings of the Railway Engineering, 2005.

[37] Jendel, T., "Prediction of wheel profile wear – comparisons with field measurements," Wear, Vol. 253, pp. 89-99, 2002.

[38] Hernandez, F. C. R., Personal Communication, October 13, 2008.

[39] Hannah, M., "Contact stress and deformation in a thin elastic layer," The Quarterly Journal of Mechanics and Applied Mathematics, Vol. 4, pp. 94 – 105, 1951.

[40] Field manual of AAR interchange rules, Rule 41, AAR, pp. 268, 2004.

[41] Federal Railroad Administration, DOT standards, pp. 230.113, 2005.

[42] Stone, D. H., and Knupp, G. G., "Rail Steels – Developments, Processing, and Use," A Symposium Sponsored by ASTM Committee A-1 on Steel, Stainless

Steel, and Related Alloys, American Society for Testing and Materials, Denver, Colorado, 17-18 Nov, 1976.

[43] Sankararaman, S., Y. Ling, and S. Mahadevan, "Model Validation and Uncertainty Quantification of Fatigue Crack Growth Analysis," Engineering Fracture Mechanics, Vol. 78, No. 7, pp. 1487-1504, 2011.

[44] Bladon, K. et al. "Predictive condition monitoring of railway rolling stock," Proceedings of the conference on railway engineering, Darwin, June 2004.

[45] Stratman, B., Liu, Y., Mahadevan, S., "Structural Health Monitoring of Railroad Wheels Using Wheel Impact Load Detectors". Journal of Failure Analysis and Prevention, Volume 7, Number 3, pp. 218-225, 2007.

[46] C. Rasmussen. Evaluation of Gaussian processes and other methods for non-linear regression. PhD thesis, University of Toronto, 1996

[47] T.J. Santner, B.J. Williams, and W.I. Noltz. (2003). The Design and Analysis of Computer Experiments. Springer-Verlag, New York, 2003.

[48] J. McFarland. Uncertainty analysis for computer simulations through validation and calibration. Ph D. Dissertation, Vanderbilt University, 2008.

[49] Liu, Y., Liu, L., Stratman, B., Mahadevan, S. "Multiaxial fatigue reliability analysis of railroad wheels," Reliability Engineering and System Safety, Vol. 93, Issue 3, pp. 456-467, 2008.

[50] Luczak, M., "Reinventing the wheel: TTCI, wheel manufacturers, reconditioners, and owners are getting a handle on new technologies to reduce the appearance of defects and increase wheel life. But could innovation be stifled?," Railway Age, June, 2004.

[51] Liu, Y., Stratman, B., and Mahadevan, S., "Fatigue crack initiation life prediction of railroad wheels," International Journal of Fatigue, Vol. 28, Issue 7, pp. 747-756, 2006.

[52] Liu, Y., Liu, L., and Mahadevan, S., "Subsurface fatigue crack propagation under rolling contact loading," Engineering Fracture Mechanics, Vol. 74, pp. 2659-2674, 2007.

[53] Sura, V. S., and Mahadevan, S., "Modeling of Vertical Split Rim Cracking in Railroad Wheels," Engineering Failure Analysis, Vol. 18, No.4, pp. 1171-1183, 2011.

[54] Sura, V. S., and Mahadevan, S., "Modeling of Shattered Rim Cracking in Railroad Wheels," Journal of Rail and Rapid Transit, 2011, accepted, in press.

[55] Sura, V., and Mahadevan, S., "Estimation of Residual Stress Distribution in Railroad Wheels," Proceedings of ASME Joint Rail Conference, Pueblo, CO, March 3-5, 2009.

[56] H. Kitagawa, R. Yuuki, Stress intensity factor of branched cracks in two dimensional stresses. Trans. Japan Society of Mechanical Engineering. Vol. 41, pg 1641-1649, 1975.